Photoactivatable senolysis with single-cell resolution delays aging

Donglei Shi[1,2,7], Wenwen Liu[3,7], Ying Gao[2,7], Xinming Li[1], Yunyuan Huang[1], Xiaokang Li[1], Tony D. James[4], Yuan Guo[2]* and Jian Li[1,3,5,6]*

[1]State Key Laboratory of Bioreactor Engineering, Shanghai Frontiers Science Center of Optogenetic Techniques for Cell Metabolism, Frontiers Science Center for Materiobiology and Dynamic Chemistry, Shanghai Key Laboratory of New Drug Design, School of Pharmacy, East China University of Science and Technology, Shanghai 200237, China.
[2]Key Laboratory of Synthetic and Natural Functional Molecule of the Ministry of Education, College of Chemistry and Materials Science, Northwest University, Xi'an 710127, China.
[3]Key Laboratory of Tropical Biological Resources of Ministry of Education, College of Pharmacy, Hainan University, Haikou 570228, Hainan, China.
[4]Department of Chemistry, University of Bath, Bath, BA2 7AY, United Kingdom.
[5]Yunnan Key Laboratory of Screening and Research on Anti-pathogenic Plant Resources from West Yunnan, College of Pharmacy, Dali University, Dali 671000, China.
[6]Clinical Medicine Scientific and Technical Innovation Center, Shanghai Tenth People's Hospital, Tongji University School of Medicine, Shanghai 200092, China.
[7]These authors contributed equally to this work.
*e-mail: guoyuan@nwu.edu.cn; jianli@ecust.edu.cn

Strategies that can selectively eliminate senescent cells (SnCs), namely senolytics, have been shown to promote healthy lifespan. However, it is challenging to achieve precise, broad-spectrum and tractable senolysis. Here, we integrate multiple technologies that combine the enzyme substrate of senescence-associated β-galactosidase (SA-β-gal) with fluorescence-tag for the precise tracking of SnCs; construction of a bioorthogonal receptor triggered by SA-β-gal to target and anchor SnCs with single-cell resolution; and incorporation of a selenium atom to generate singlet oxygen and achieve precise senolysis through controllable photodynamic therapy (PDT). We generate KSL0608-Se, a photosensitive senolytic prodrug, which is selectively activated by SA-β-gal. In naturally-aged mice, KSL0608-Se-mediated PDT prevented upregulation of age-related SnCs markers and senescence-associated secretory phenotype factors. This treatment also countered age-induced losses in liver and renal function as well as inhibited the age-associated physical dysfunction in mice. We therefore provide a strategy to monitor and selectively eliminate SnCs to regulate aging.

Aging is the leading risk factor associated with numerous pathologies, including cancer and fibrosis[1-3]. A fundamental aging mechanism has been proposed to be linked to the excessive, usually time-dependent, development of cellular senescence, a stable and stagnant terminal state that occurs after stress-induced cellular damage[1,4]. This accumulation drives inflammation-mediated tissue dysfunction and aging by promoting the secretion of proinflammatory and matrix-degrading molecules (known as the senescence-associated secretory phenotype, SASP)[5,6]. The selective removal of senescent cells (SnCs), termed "senolysis", can alleviate these age-related features and extend the healthy lifespan, as supported by recent investigations in mice[7], leading to an exploration of therapeutic approaches towards senolysis[8-13].

Surgical removal of aging tissue is currently used as a therapeutic approach for the motor dysfunction caused by the accumulation of SnCs. However, because this treatment is limited to muscle aging and causes trauma and pain to patients, a better approach would be to selectively eliminate SnCs with senolytic drugs (senolytics). Senolytics were initially selected based on their ability to transiently switch off senescence-associated antiapoptotic pathways[14-18]. Typical examples include ABT-737 and ABT-263, which target SnCs to induce apoptosis by inhibiting antiapoptotic proteins in the BCL-2 family[8,19-22]. Some natural senolytics, such as quercetin and fisetin, have also proved effective in influencing aging and age-related diseases[16,23-25]. However, SnCs exhibit great heterogeneity and dynamics *in vivo*[9,10,26-28], resulting in significant limitations of these senolytics in terms of accuracy (no toxicity to non-SnCs), tractability (administration controllability) and broad-spectrum activity (effectiveness against different types of SnCs). Even though there are emerging strategies to address these issues, including glutaminolysis inhibition[26] and enzyme-targeted prodrugs[9,10], to the best of our knowledge, no report has described a smart, senotherapeutic agent able to achieve all these aims.

The integration of multiple technologies is an appealing way to achieve the development of such desirable senolytics. Photodynamic therapy (PDT) is a contemporary therapeutic technique that can destroy target cells by

activating a photosensitive drug with the aid of a light source[29-32], which offers the potential to improve the tractability of senolytics due to the dependence on light illumination. Meanwhile, the prodrug strategy targeting senescence-associated β-galactosidase (SA-β-gal) for senolysis has shown advantages in broad-spectrum activity since the enhanced activity of this enzyme is a common feature of SnCs[9,33,34]. A further challenge in the targeting of small-molecule drugs in general is that they readily exit their target cells due to rapid transport across cell membranes and enter the surrounding normal cells due to free diffusion. The utilization of emerging anchoring technologies that can covalently bind drugs to sites of interest through bioorthogonal reactions[35-40] could limit such off-target effects.

Accordingly, we here report the construction of a smart senotherapeutic agent, **KSL0608-Se**, that integrates PDT with β-gal-targeted prodrug and target-site anchoring technologies to achieve tractable, broad-spectrum activity and accuracy. This integrated strategy enables the selective activation of **KSL0608-Se** by SA-β-gal to form a bioorthogonal receptor (quinone methide). The active receptor covalently reacts with exposed nucleophilic groups (e.g., sulfhydryls) on the surfaces of surrounding proteins, converting the prodrug into a near-infrared (NIR)-emitting senolytic drug. The bioorthogonal reaction and fluorescence off-on behaviour occur only after activation by SA-β-gal, which allows selective monitoring of and precise anchoring to SnCs. The newly formed drug can be activated by light *in situ* to produce singlet oxygen in SnCs, resulting in photocontrollable senolysis at single-cell resolution. **KSL0608-Se** achieved the specific recognition and selective clearance of SnCs in a complex coculture system of young cells and SnCs. Of note, in naturally aged mice and mice treated with doxorubicin (doxo), the **KSL0608-Se**-guided therapy effectively decreased the number of SA-β-gal-positive cells and inhibited the expression of age-related genes and markers. This treatment also showed the ability to improve age-associated physical dysfunctions in naturally aged mice. In brief, our unprecedented integration strategy can effectively eliminate SnCs and exhibit the potential to counteract aging and ameliorate age-related diseases.

Results

Design of a photoactivatable prodrug for senolysis. Our main focus in designing this senolytic prodrug was ensuring the accurate delivery of the photosensitive drug to SnCs for precise and controllable yet complete senolysis with single-cell resolution. We then report a prodrug strategy to design a photosensitive senolytic agent activated by SA-β-gal, an enzyme both specific to and widespread among SnCs. The synthesis starts with the modification of a dicyanomethylene-4H-pyran (DCM) based skeleton with favorable donor–π–acceptor (D–π–A) characteristics and a phenolic group for regulating electron-donating capability (Fig. 1a). We then replaced the oxygen (O) atom on the skeleton with a selenium (Se) atom to enhance singlet oxygen generation upon photoirradiation. It is believed that this effect is attributed to the increase in molecular dipoles and the enhanced intersystem crossing ability (ISC)[30,41,42]. To this photosensitive scaffold, a β-D-galactosyl group was attached as both the SA-β-gal-responsive site and the phototoxicity blocking group, and a fluoromethyl was added as a self-immobilizing moiety, creating the photosensitive prodrug **KSL0608-Se**. This prodrug is converted to a bioorthogonal quinone-methide receptor *via* a 2-fluoromethylphenol intermediate immediately after its specific hydrolysis by SA-β-gal. This receptor is unique in that it can covalently attach to nearby proteins and selectively generate a photosensitive drug *in situ* in SnCs (Fig. 1b). Based on the same design strategy, a self-immobilizing SA-β-gal fluorescent probe with O instead of Se, **KSL0608-O**, was synthesized (Fig. 1a). After hydrolysis by SA-β-gal, **KSL0608-O** exhibits fluorescence similar to **KSL0608-Se** but does not produce a phototoxic substance, thus it is also a desirable control. Accordingly, **KSL0608-O** and **KSL0608-Se** were synthesized as outlined in Fig. 1a, described in more detail in the Supplementary Information (Section "Synthesis and characterization" and Supplementary Figs. 12-55).

Spectral response towards β-galactosidase (β-gal). The fluorescence spectra and the absorption spectra of **KSL0608-O** and **KSL0608-Se** were evaluated. *E. coli* β-gal, as the SA-β-gal model protein, was used in catalytic amounts for substrate recognition, and bovine serum albumin (BSA), with a strongly nucleophilic sulfhydryl group[43], was supplied in excess in the recognition system to provide a model protein substrate for the reaction with the quinone-methide receptor. As expected, prior to treatment with *E. coli* β-gal and BSA, both **KSL0608-O** and **KSL0608-Se** exhibited faint fluorescence since the hydroxyl group was caged by a β-D-galactosyl group, suppressing the intramolecular charge transfer (ICT) process. After treatment with *E. coli* β-gal, both compounds exhibited negligible fluorescence changes. However, in the presence of BSA, the addition of *E. coli* β-gal stimulated a significant fluorescence increase at 665 nm for **KSL0608-O** and at 721 nm for **KSL0608-Se** (Fig. 2a,b). In addition, the absorption spectra exhibited a red-shift upon the addition of both *E. coli* β-gal and BSA (Supplementary Fig. 1). To our delight, the addition of BSA into the **KSL0608-O/Se** system provoked a large fluorescence enhancement, while adding other nucleophilic small molecules did not (Extended Data Fig. 1a,b). This should be attributed to the enhanced rigidity of the fluorophore after binding with proteins like BSA, although these small-molecule species can also react with the quinone-methide receptor. Furthermore,

SDS-PAGE and in-gel fluorescence imaging were performed to confirm that both compounds could covalently modify proteins after enzymatic activation. An intense fluorescent band was observed at the expected molecular weight for BSA in the group containing **KSL0608-O**/**KSL0608-Se**, *E. coli* β-gal and BSA (Fig. 2c). In contrast, no fluorescence signal was observed in the absence of BSA or *E. coli* β-gal. These results confirm that the hydrolysis of the two compounds by *E. coli* β-gal leads to the formation of fluorescent adducts through electrophilic intermediates capable of covalently reacting with surrounding proteins.

Emission titration experiments of both compounds with *E. coli* β-gal at different concentrations were then conducted. A dramatic increase in the NIR fluorescence of **KSL0608-O** at ~665 nm was elicited by *E. coli* β-gal, and a linear relationship between fluorescence intensity and *E. coli* β-gal concentration was observed, with a correlation coefficient (R^2) greater than 0.96 (Fig. 2d). Similarly, upon the addition of *E. coli* β-gal, an increase in the NIR fluorescence of **KSL0608-Se** at ~721 nm appeared, again with a good linear relationship ($R^2 > 0.99$) (Fig. 2e). Accordingly, the limits of detection (LOD) of β-gal by **KSL0608-O** and **KSL0608-Se** were calculated to be 3.12×10^{-3} U/mL and 8.96×10^{-2} U/mL, respectively (Supplementary Table 1). Furthermore, a molecular docking simulation of **KSL0608-O** with human β-gal (PDB: 3THC) was performed. Multiple hydrogen bonds form between the galactosyl group of **KSL0608-O** and human β-gal, and the binding model significantly overlaps with that adopted by galactose (Fig. 2f,g), suggesting that **KSL0608-O** could be fully hydrolyzed by human β-gal to release the active precursor. The above results indicated that both compounds could be activated by β-gal and immobilized on proteins of interest *in situ*, suggesting their ability to monitor fluctuations in β-gal and the feasibility of our SA-β-gal-activatable prodrug and target-site anchoring design strategy.

The reaction kinetics of **KSL0608-O** and **KSL0608-Se** with β-gal were further investigated. After the addition of *E. coli* β-gal and BSA, the fluorescence intensity for the two compounds was markedly enhanced and reached a maximum within 10 min (Extended Data Fig. 1c,d). Additionally, the effect of pH on the fluorescence response of **KSL0608-O**/**KSL0608-Se** to β-gal over a wide pH range (4-10) was then investigated. Both compounds were stable and displayed a good response to β-gal over this pH range, ensuring their ability to track β-gal at physiological pH (Extended Data Fig. 1e,f). Next, their photostability for the detection of β-gal was evaluated and the results indicated that both compounds exhibit high photostability and the potential to track β-gal over a long duration *in vivo* (Extended Data Fig. 1g,h).

Photoinduced ROS generation *in vitro*. We then examined the ability of **KSL0608-O** and **KSL0608-Se** to convert oxygen into reactive oxygen species (ROS) after photoirradiation using a commercial ROS indicator 1,3-diphenlisobenzofuran (DPBF)[44-47]. Under light irradiation, the absorption of DPBF remained constant in the presence of **KSL0608-O** or **KSL0608-Se** alone, implying that neither triggers ROS generation associated toxicity even when exposed to light (Fig. 2h). In contrast, the absorption of DPBF in the group containing **KSL0608-Se**, *E. coli* β-gal and BSA decreased rapidly within 1 min, confirming the efficient generation of ROS once **KSL0608-Se** was activated (Fig. 2h,i). Conversely, no significant change was observed in that of the group containing **KSL0608-O**, *E. coli* β-gal and BSA, indicating that replacement of the Se atom with an O atom significantly decreased the ability to generate ROS. Consistent with this, the singlet oxygen quantum yields (Φ_Δ) of **KSL0608-O** and **KSL0608-Se** were calculated to be 0.07 and 0.20 and their relative fluorescence quantum yields (Φ_{fl}) were 0.33 and 0.08, after the addition of *E. coli* β-gal and BSA (Supplementary Table 1). These results confirmed that **KSL0608-Se** does not produce ROS by itself, but can generate an effective photosensitive drug *in situ* after being triggered by the target protein.

Endogenous β-gal imaging in live cells. Prior to cell imaging, the cytotoxicity of our compounds was evaluated and both compounds exhibited low cytotoxicity (Supplementary Fig. 2). Human ovarian cancer cells (SKOV3) with high endogenous β-gal levels, and human liver cancer cells (HepG2) containing low endogenous β-gal, were incubated separately with our compounds. A marked NIR fluorescence signal was observed in SKOV3 cells, whereas no significant fluorescence signal appeared in HepG2 cells (Extended Data Fig. 2a,b). D-galactose and phenylethyl β-D-thiogalactopyranoside (PETG), two kinds of β-gal inhibitor[48,49], were used to reduce the activity of β-gal in cells. As expected, after treatment with each inhibitor, SKOV3 cells incubated with **KSL0608-O**/**KSL0608-Se** displayed reduced fluorescence in the NIR channel (Extended Data Fig. 2c,d), supporting the specificity of both compounds for detecting endogenous β-gal in live cells.

We then evaluated their capability to monitor β-gal activity in senescent normal cells and senescent cancer cells, including human lung fibroblastic cells (MRC-5) with replication-induced senescence, and rat renal tubular epithelial cells (NRK-52E), human non-small lung cancer cells (A549) and normal human liver cells (HL-7702) with a senescent phenotype mediated by DNA damage. Such senescent cells with DNA damage were obtained by stimulations with ROS for NRK-52E, Mitomycin C (MitoC) for A549 and doxo for HL-7702[14,15]. After incubation with **KSL0608-O** or **KSL0608-Se**, all the senescent cells emitted stronger NIR fluorescence than the corresponding young cells with low expression of β-gal (Fig. 3a-c). The results of X-gal staining and western blot

assays for p21 and p53 of young cells and SnCs were in good agreement with the above results (Fig. 3a and Supplementary Fig. 3). These results confirmed that both compounds could monitor SA-β-gal in live cells.

Lysosome-targeted function of KSL0608-O and KSL0608-Se. Senescent MRC-5 cells (P40) were co-incubated with **KSL0608-O** or **KSL0608-Se** and commercial staining dyes targeting different organelles. The NIR fluorescence overlapped well with the green fluorescence of LysoTracker in senescent MRC-5 cells. In contrast, there was poor overlap between the fluorescence in the NIR channel and that in the green channel for MitoTracker or GolgiTracker (Fig. 3d,e and Supplementary Fig. 4). These results indicated that our molecules responsible for NIR fluorescence accumulated mainly in the lysosomes of SnCs, suggesting that they can function *in situ* through enzymatic reaction with the endogenous SA-β-gal located in lysosomes.

Light-controllable removal of SnCs in a coculture system. We chose a safe dose (12 J/cm^2) for the following PDT experiments in living cells (Extended Data Fig. 3a-d) and confirmed the ability of this dose of light to induce ROS (Fig. 4a,b). From Fig. 4c, upon light irradiation, **KSL0608-Se** exhibited the specific dose-dependent phototoxicity to these senescent cells at 24 h. Through our treatment, over 65% of the drug-induced senescent cells were killed. The **KSL0608-Se**-mediated PDT also exhibited phototoxicity towards P40 MRC-5 cells whose senescence degree was higher than that of MRC-5 cells at P28 (Fig. 4c). We next test its cytotoxicity at 48 h and 72 h and found that no significant toxicity to all the young cells appeared (Extended Data Fig. 3e-l). Of note, upon the prolonged incubation time, this treatment is a little phototoxic to MRC-5 cells at P28, not a low passage for normal cells, but the phototoxicity was far lower than that to more senescent MRC-5 cells (P40) (Extended Data Fig. 3h,l). Furthermore, no dark cytotoxicity was observed in both young and senescent cells within 3 days after treatment. The above cytotoxicity test results supported our claim of the photoactivatable senolysis (Extended Data Fig. 4). Flow cytometry analysis using Annexin V/PI double staining was used to further confirm the selective phototoxicity of our treatment to SnCs. As expected, we observed the number of apoptotic cells among the MRC-5 cells (P40) higher than that among the MRC-5 cells (P28) (Fig. 4d,e). Interestingly, the **KSL0608-Se**-mediated PDT was desirably only sensitive to the RAW264.7 cells (a macrophage with a certain β-gal expression ability) matured by drug induction, but not to the uninduced RAW264.7 cells (Supplementary Fig. 5), which can be explained by the overexpression of β-gal in macrophages occurred only at the mature stage[50]. Such *in-vitro* treatment on cells was conducted in PBS buffer without serum, which is a culture condition of nutrient starvation with the risk of evoking cell autophagy. Thereby we evaluated effects of PBS on cells. All the results indicated that PBS had negligible cytotoxicity and did not cause cell autophagy within the treatment time we used (Supplementary Fig. 6), driving out this risk.

To further verify the specificity of **KSL0608-O** and **KSL0608-Se** to SnCs, a coculture system of SnCs and young cells was built (Extended Data Fig. 5a,b), in which young cells were prelabelled with green fluorescence and then cocultured with SnCs. As shown in Fig. 4f,g and Extended Data Fig. 5c-f, the young cells exhibited negligible fluorescence in the NIR channel, whereas SnCs displayed bright NIR fluorescence, achieving the specific labelling of SnCs. We then investigated the ability of the two compounds to specifically kill SnCs in this coculture system. Cocultured cells were treated with **KSL0608-Se** accompanied by irradiation, and the more senescent MRC-5 cells (P40) exhibited significant cell shrinkage and morphological changes that are characteristic of apoptosis (Fig. 4g); however, the MRC-5 cells (P28) remained unchanged in shape. When **KSL0608-O** was used instead of **KSL0608-Se**, neither the P28 MRC-5 cells nor the P40 MRC-5 cells underwent a change in cell shape (Fig. 4f). These results indicated that both compounds possess the ability to recognize and target SnCs, while **KSL0608-Se** is unique in its capacity to selectively kill SnCs. Furthermore, from Supplementary Fig. 7, multiple fluorescent bands were observed over a wide molecular weight range for the senescent HL-7702 cells incubated with **KSL0608-O** or **KSL0608-Se**, illustrating that the NIR-emitting products were formed and successfully anchored to a variety of proteins in SnCs.

Whole-body fluorescence imaging of SnCs *in vivo*. Probe **KSL0608-O** can be activated and then emit bright fluorescence under the excitation of light at almost the same wavelength as **KSL0608-Se**. This allows the use of **KSL0608-O** in the *in-vivo* fluorescence imaging experiments in mice to verify the penetration ability of the irradiation light used in the **KSL0608-Se**-mediated PDT to solid organs. As shown in Fig. 5a,b, the fluorescence intensity in the abdomen of aged mice gradually increased over time and reached up to a maximum at 96 h, whereas it was negligible in that of young mice, supporting the targeting activation of **KSL0608-O** in aged mice. Additionally, the fluorescence intensity of liver, lung and kidney gained from aged mice was stronger than that from young mice, whereas the heart and spleen from both aged and young mice displayed negligible fluorescence signal (Fig. 5c,d), suggesting senescence mainly occurs in liver, lung and kidney of these aged mice. These results provided the evidence that the irradiation light used in **KSL0608-Se**-mediated PDT has the ability to penetrate tissues.

Selective removal of SnCs in a mouse model with doxo-induced senescence. We next evaluated the PDT effect of **KSL0608-Se** *in vivo* against age-related pathologies (Fig. 6a). Various aging markers to evaluate the anti-aging efficacy of **KSL0608-Se**-mediated PDT for senolysis were investigated. We assessed the expression levels of γ-histone-2AX (γ-H2AX), a recognized age-related marker[51,52]. The results indicated that our treatment reduced the expression of γ-H2AX in the livers and kidneys of aged mice (Fig. 6b). Serum biochemical tests showed that the aging induced upregulation of aspartate aminotransferase (AST) and alanine aminotransferase (ALT) as age-associated indicators[53-55] was counteracted (Fig. 6c). In addition, the PDT treatment with **KSL0608-Se** markedly decreased the expression level of *p21* and *IL-1β*, two other markers for aging[8,53] (Fig. 6d and Supplementary Fig. 8). Consistent with this observation, the expression level of SA-β-gal, as detected by both X-gal and **KSL0608-O** staining, indicated that there were markedly fewer SnCs in the kidneys of aged mice after **KSL0608-Se**-mediated PDT (Fig. 6e). Such results support that our treatment could effectively remove SnCs to inhibit the upregulation of different age-related markers in aged mice.

RNA sequencing of the livers from these mice was carried out. Comparison of the gene expression in the young control group and aged control group revealed 362 differentially expressed genes (Fig. 6f,g). There were 656 differentially expressed genes between the "**KSL0608-Se** + irradiation" group and the aged control group (Fig. 6f,g). The 128 genes that were differentially expressed in both comparisons were analyzed (Supplementary Fig. 9). As shown in Fig. 6h, 27 genes associated with deleterious effects of aging (SASP and fibrosis phenotypes) were upregulated in doxo-treated mice and downregulated following PDT with **KSL0608-Se**. In addition to these 128 genes, 4 genes known to be associated with aging displayed similar but nonsignificant changes in expression. These results strongly support **KSL0608-Se** as a desirable senotherapeutic agent able to delaying aging in mice by reversing the expression of aging-related genes.

Selective removal of SnCs in a naturally aged mouse model. The related experiments were then carried out in naturally aged mice (Fig. 7a). We first tested the levels of age-related indicators in the kidneys and livers of mice in the four groups. The results of western blot analysis indicated the expression level of p53 from the "**KSL0608-Se** + irradiation" group was significantly reduced while that from the **KSL0608-Se** group did not decrease so much (Fig. 7b). We then found that p21 and SA-β-gal positive SnCs from the "**KSL0608-Se** + irradiation" group was much less than those from the aged control group (Fig. 7c,d). Subsequently, we also found the level of uric acid (UA), creatinine (Cr), blood urea nitrogen (BUN), ALT and AST increased in aged mice (Fig. 7e,f). To our delight, the expression level of these indicators in mice from the "**KSL0608-Se** + irradiation" group was downregulated, demonstrating that our treatment could counteract the age-associated loss of renal function and liver function. Notably, the expression of key SASP factors in livers, kidneys and serum, including CXCL1, CXCL3, IL-1β, IL-6, MMP-1, MMP-7 and TNF-α, increased with age and was significantly reduced after our treatment (Fig. 8a-g and Extended Data Fig. 6a-n). Additionally, p16, a cell cycle regulator whose expression level increased with age, also decreased in level after treatment (Extended Data Fig. 6o). From these results, the treatment used in the "**KSL0608-Se** + irradiation" group exhibited the more powerful ability to decrease the level of all these indicators compared to that in the **KSL0608-Se** group, establishing the irreplaceable role of irradiation in the treatment. Additionally, the results of hematoxylin and eosin (H&E) staining assay confirmed our no-toxic treatment to the main organs of mice (Supplementary Fig. 10). The **KSL0608-Se**-mediated PDT showed an effective photoactivatable senolysis in livers and kidneys of naturally aged mice, and thus successfully ameliorated the age-associated losses of such organs.

Naturally aged mice showed significant declines in muscle strength, hanging endurance, locomotor activity and walking speed, time and distance, while all of which were recovered after treatment with **KSL0608-Se**-mediated PDT (Fig. 8h-k and Supplementary Fig. 11). As a control, no obvious signs of recovery in mice from the **KSL0608-Se** group were observed. Additionally, there were no significantly cognitive alterations in all groups of mice (Fig. 8k), further supporting the safety of our treatment. To be brief, our **KSL0608-Se**-mediated PDT could markedly improve the decline symptoms of naturally aged mice in physical function.

We then carried out the RNA sequencing analysis of differentially expressed genes in the mouse livers. By comparing the gene expression in the young control group with that in the aged control group, 1399 differentially expressed genes were found (Fig. 8l,m). While 578 differentially expressed genes were observed between the aged control group and the "**KSL0608-Se** + irradiation" group (Fig. 8l,n). As shown in Fig. 8l and Extended Data Fig. 7, there were 146 common genes in these two groups of differentially expressed genes. Among them, after **KSL0608-Se**-mediated PDT, 18 age-related genes upregulated with age were downregulated and 6 genes downregulated with age were upregulated (Fig. 8o). Another 10 genes upregulated with age, which are associated with SASP and fibrosis phenotypes, also were downregulated after our treatment (Fig. 8o). The successful modulation of these age-related genes further confirmed the reliability of our treatment strategy in delaying natural aging.

Discussion

We present a general strategy to construct senolytics, which combines the advantages of tractability, broad-spectrum activity, and accuracy through the integrated use of PDT, β-gal-targeted prodrug and target-site anchoring technologies. Using the strategy, we generated a smart senolytic prodrug, **KSL0608-Se**, that is capable of being selectively activated by SA-β-gal and then bioorthogonally anchored to nearby proteins in SnCs. This results in the *in situ* formation of a photosensitive drug with the capability of generating highly cytotoxic $^1O_2$ and emitting fluorescence in the NIR region, facilitating the fluorescence-guided photoactivatable senolysis with single-cell resolution. We also developed **KSL0608-O** with O rather than Se as both a control molecule and an excellent self-immobilizing NIR-emitting probe for the precise imaging of senescence *in vivo.* Compared with **KSL0608-O**, **KSL0608-Se** exhibited a weaker fluorescence response but stronger phototoxicity towards SnCs, confirming that the introduction of the Se atom was key to improving photosensitivity.

Cell imaging studies confirmed that **KSL0608-Se** can be activated specifically to emit NIR fluorescence in different types of SnCs and exhibits the ability to distinguish SnCs from young cells. Importantly, cytotoxicity and flow cytometry assays confirmed low dark toxicity of **KSL0608-Se** to both young cells and SnCs but high phototoxicity to SnCs. From these results, **KSL0608-Se** exhibits high efficiency against different types of SnCs (broad-spectrum activity) and minimal side effects to nonirradiated areas (tractability). In an *in vitro* coculture system of SnCs and young cells to mimic the aging environment, we observed that only SnCs exhibited non-negligible NIR emission and were destroyed after **KSL0608-Se**-mediated PDT for 1 h, confirming the accurate fluorescence-guided senolysis by **KSL0608-Se** (precision). In both the X-gal and fluorescence imaging assays of the kidneys of doxo-treated mice, **KSL0608-Se** proved efficient at reducing the percentage of SA-β-gal-positive cells. Western blot assays confirmed that the expression levels of the aging marker γ-H2AX were significantly decreased in the kidney and liver tissues from the "**KSL0608-Se** + irradiation" group. In addition, the aging markers *p21* and *IL-1β*, and the liver damage indicators AST and ALT, were inhibited after **KSL0608-Se**-mediated PDT according to the results of RT-qPCR and serum tests. Consistent with these results, we found through RNA sequencing that our treatment attenuated the expression of 31 senescence-associated genes in livers of the doxo group. We further tried treating naturally aged mice whose aging symptoms are usually more difficult to be improved than those of the mice with drug-induced senescence. As evident from the results of X-gal and IF assays, the **KSL0608-Se**-mediated PDT successfully eliminated the SnCs in livers and kidneys of the naturally aged mice. Our treatment also desirably inhibited the upregulation of various age-related markers, which was supported by the results of western blot and ELISA assays. In addition, it played the counteraction against the age-induced losses in liver function and renal function and achieved the recovery of the age-associated physical dysfunctions. Most notably, 34 key age-related genes in livers of naturally aged mice were inhibited, suggesting the powerful ability of our strategy to treat signs of natural aging.

These successes in mice confirm our strategy to monitor and selectively eliminate SnCs to regulate aging. Since our treatment regime is photoactivated and thus non-invasive, the biological effects depend on the wavelength of the light irradiation absorbed by the photosensitive drug. One major concern is that for translation of this treatment for deep tissues and organs of larger species the 535 nm light irradiation used could result in limited tissue penetration, nevertheless we believe that **KSL0608-Se** can be successfully applied for the PDT of skin, muscle and superficial organs of large species. With our future research we intend to extend the absorption wavelength of the photosensitive drug to the NIR region enabling improved tissue penetration to facilitate full body treatment of larger species.

Overall, our results indicate that **KSL0608-Se** is a potent senolytic drug with the advantages of tractability, broad-spectrum activity, and precision. The unprecedented integrated strategy provides a paradigm for the development of senolytics that can overcome the limitations of regular senolytics. Another crucial insight that has emerged from our research is that PDT as an approach for senolysis and scavenging SnCs has numerous advantages over traditional senolytics, particularly if it is based on the integrated use of emerging technologies for the design of senolytic agents. As such, our strategy not only provides a route for eliminating SnCs but also provides the basis for PDT to precisely regulate aging.

Methods

Statement of ethical regulations. All animal experiments were performed in accordance with institutional guidelines and were approved by the Institutional Animal Care and Use Committees of Tongji University in compliance with Chinese law for experimental animals with an approval number of SYXK (Shanghai) 2020-0002.

Preparation of the spectral measurements. **KSL0608-O** and **KSL0608-Se** were respectively dissolved in DMSO to obtain stock solutions (1 mM) and diluted to 10 μM for all spectral studies. *E. coli* β-gal was dissolved in phosphate buffer saline (PBS) buffer (pH = 7.4, 10 μM) to obtain 10 U/mL stock solutions. Similar, stock solutions of BSA (10 mg/mL) were prepared in PBS buffer (pH = 7.4, 10 mM). PBS buffers with different pH values including 4.74, 5.66, 6.86, 7.40, 8.05, 8.68 and 10.07 were prepared using

standard procedures. Absorption and fluorescence spectra of those compounds with *E. coli* β-gal were performed at 37 ºC in a 2 mL total volume of PBS buffer (10 μM, pH 7.4) containing 1 mg/mL BSA in a 1 cm cuvette.

Calculation of the LOD. The LOD was determined from the fluorescence titration data based on an acknowledged method. The plots of fluorescence intensity of **KSL0608-O** and **KSL0608-Se** toward different concentrations of *E. coli* β-gal, all showed a good linear relationship (with R^2 greater than 0.96), and the LOD was calculated using the following equation:

$$\mathrm{LOD} = 3\sigma/k$$

where σ is the standard deviation of eleven blank measurements and k is the slope of the linear equation.

Calculation of the Φ_{fl}. The Φ_{fl} of **KSL0608-O**/**KSL0608-Se** before and after the addition of *E. coli* β-gal and BSA was determined by comparison with the fluorescence of fluorescein ($\Phi_{fl,st}$ = 0.95 in 0.1 M NaOH). The Φ_{fl} was calculated according to following equation[56]:

$$\Phi_{fl,x} = \Phi_{fl,st}\left(\frac{F_x A_{st}}{F_{St} A_x}\right)$$

where subscripts *x* and *st* represent the sample to be tested, respectively. *F* is the integrated fluorescence emission. *A* represents the absorbance of compound at its respective excitation wavelengths.

Calculation of the Φ_{Δ}. The Φ_{Δ} was determined using chlorin e6 (Ce6) as a reference and 1,3-diphenylisobenzofuran (DPBF) as a ROS trapping agent. DPBF (abs < 1.00), and **KSL0608-O** or **KSL0608-Se** (10 μM) were added in a cuvette containing air-saturated solvents and the solutions were kept in the dark until the absorbance reading was stable, followed by continuous light irradiation (535 nm, 10 mW/cm^2) at 5 s intervals. The Φ_{Δ} was calculated by following equation[57,58]:

$$\Phi_{\Delta,x} = \Phi_{\Delta,st}\left(\frac{S_x}{S_{st}}\right)\left(\frac{F_{st}}{F_x}\right)$$

where subscripts *x* and *st* represent the sample to be tested and the standard reference Ce6 ($\Phi_{\Delta,st}$ = 0.65), respectively. *S* is the slope of the absorption curve of DPBF at the wavelength of 410 nm over time. *F* is the absorption correction factor, which is given by F = $1–10^{-OD}$ (OD represents the optical density of sample and Ce6 at 535 nm).

Cell culture. MRC-5 cells, HepG2 cells, RAW264.7 cells, A549 cells and SKOV3 cells were purchased from Cell Bank of Chinese Academy. HL-7702 cells were purchased from Shanghai FuHeng BioLogy Co., Ltd. NRK-52E cells were purchased from Procell Life Science&Technology Co., Ltd. MRC-5 cells were cultured in MEM (Gibco) supplemented with 10% FBS (Gibco), 1% penicillin/streptomycin (Yeasen), 1 mM sodium pyruvate solution (BI), and 1% non-essential amino acids solution (BI). SKOV3 cells, A549 cells and HL-7702 cells were cultured in RPMI-1640 (HyClone) medium supplemented with 10% FBS and 1% penicillin/streptomycin. NRK-52E cells, RAW264.7 cells and HepG2 cells were cultured in DMEM (Gibco) medium supplemented with 10% FBS and 1% penicillin/streptomycin. All cells were cultured and maintained at 37 °C with 5% CO_2. To obtain drug-induced senescent cells, A549 cells were stimulated with MitoC (0.5 μM) twice for two days and HL-7702 cells were treated with doxo (1 μM) for 1 day. NRK-52E cells were stimulated with 150 nM H_2O_2 for 1 day and cultured for 2 days to induce senescence. To obtain mature RAW 264.7 cells, RAW 264.7 cells were stimulated by Lipopolysaccharide (Lps, 50 ng/mL) and interferon-γ (INF-γ, 100 ng/mL) for 3 days[59].

Cytotoxicity assay. The percentage cell survival of these cells after treatment with **KSL0608-O** or **KSL0608-Se** was assessed by using a Cell Counting Kit-8 (CCK-8) assay. Cells were seeded into a 96-well plate at 6000 cells per well and treated with **KSL0608-O** and **KSL0608-Se** at different concentrations for 24 h. For irradiation experiment, the cells were separately incubated with **KSL0608-Se** in PBS buffer for 30 min, followed by irradiation with an LED lamp (535 nm, 10 mW/cm^2) for 20 min. Then, the PBS buffer was removed from the petri dish and the culture medium was added into the dish, the cells were further incubated in the incubator for 24 h, 48 h and 72 h, respectively. As a control experiment, all these cells were treated with PBS buffer for different times. Then the PBS buffer was replaced by the culture medium and further incubated in the incubator for 24 h. For cytotoxicity tests, the culture medium was removed, 10 μL of CCK-8 solution was added to each well, and the 96-plates were incubated at 37 °C with 5% CO_2 for 2 h. A Microplate Reader (Bio-Tek Instruments, Synergy H1) was employed to record the absorbance of each well at 450 nm. The percentage cell survival was evaluated by measuring the absorbance at 450 nm and calculated by the formula (percentage cell survival = $(OD_{positive} - OD_{control})/(OD_{negative} - OD_{control})$). All experiments were carried out at least in triplicate.

Influences of autophagy process. To ensure the reliability of our treatment, we have further evaluated the cytotoxicity of PBS on senescent/young cells at different treatment times. The cells were treated with PBS buffer for different times and the cytotoxicity of PBS to these cells was evaluated by CCK8 assays. **AF-C**, an autophagy-pH-sensitive ratiometric fluorescence probe[60,61], was used to monitor the autophagy process of cells in PBS buffer within 2 h. The PBS-treated cells were incubated with **AF-C** (20 μM) for 15 min and then imaged by a Leica TCS SP8 SMD confocal microscope.

Confocal imaging. Cells were plated on a glass-bottomed cell culture dish (NEST Biotechnology, 801001) and incubated with normal medium for 1-2 days. Then, the medium was replaced with PBS buffer containing 10 μM (or 5 μM) probe (**KSL0608-O** or **KSL0608-Se**) and incubated for 30 min. Then the above cells were washed with PBS for three times. The tissue sections were immersed in a PBS buffer containing 10 μM probe (**KSL0608-O**) for 1 h at 37 °C, and then washed with PBS buffer and mounted with 75% glycerol. The fluorescence imaging of cells and tissue sections were performed by a Leica TCS SP8 SMD confocal microscope and a Nikon csu-w1 sora confocal microscope, respectively.

MRC-5 cells (P28) and young HL-7702 cells were stained with 5 μM CellTracker Green CMFDA (Yeasen, 40721ES50) for 20 min, respectively. The above CMFDA-stained young cells and senescent cells were co-cultured for 1 day. Then, the co-cultured cells were incubated with **KSL0608-O** (10 μM) or **KSL0608-Se** (10 μM) for 30 min and fluorescence imaging was carried out.

X-gal staining assay. Cultured cells were washed with PBS once and fixed for 10 min at room temperature in 4% formaldehyde and 2% glutaraldehyde. Then, after washing three times with PBS, MRC-5 cells, HL-7702 cells, A549 cells, NRK-52E cells were respectively incubated with SA-β-gal staining solution (1 mg/mL X-gal, pH = 6.0) overnight at 37 °C and RAW 264.7 cells were incubated with β-gal staining solution (1 mg/mL X-gal, pH = 4) for 7 h at 37 °C. Additionally, the frozen sections were dried at 37 °C for 15 min and then fixed with 2% formaldehyde and 0.2% glutaraldehyde in PBS for 10 min. Subsequently, the sections were washed with PBS for three times and then incubated with 1 mg/mL X-gal staining solution (pH = 6.0 for kidney sections, pH = 4.0 for liver sections[62]) overnight at 37 °C. After completion of β-gal staining, the sections were washed using PBS for three times. The images of X-gal-staining were collected using a Ti-S microscope (Nikon).

Flow cytometric assay. MRC-5 cells were seeded in culture plates and were cultured for 24 h. Then the cells were incubated with **KSL0608-Se** (10 μM) for 30 min and then were exposed under an LED lamp (535 nm, 10 mW/cm^2) for 20 min. Cells were further cultured for 5 h and were digested by trypsin-EDTA solution. Finally, the above cells were washed with PBS, and stained with PI and Annexin V-FITC following the protocol (Bytotime Biotechnology, C2015M). Then the samples were analyzed by flow cytometry (CytoFLEX LX, Beckman Coulter, CA, USA).

Drug treatment *in vivo*. C57BL/6J mice (male and female, 2-month-old and 21-month-old) were purchased from Charles River Laboratory Animal Co., Ltd, maintained under specific pathogen-free facility (SPF) at 25 °C and 40-60% humidity conditions with a 12 h light/12 h dark cycle and free access to food and water.

KSL0608-O or **KSL0608-Se** was mixed in mixture solution containing 70% normal saline, 25% castor oil and 5% DMSO. Doxo was dissolved in normal saline. All drugs were administered to the mice by intraperitoneal (i.p.) injection.

To construct mouse model with doxo-induced senescence, doxo (3 mg/kg) was administrated to mice (male) once on the day 1 and day 10. Then, **KSL0608-Se** (20 mg/kg) was administrated to aged mice on the day 24. And the mice were sacrificed on thirty-eighth day. For young mice and naturally aged mice (female), mice were divided into the young (2-month-old) control group, the aged (21-month-old) control group to be treated with vehicle, the **KSL0608-Se** group (21-month-old) to be treated with **KSL0608-Se** (10 mg/kg), and the "**KSL0608-Se** + irradiation" group (21-month-old) to be treated with both **KSL0608-Se** (10 mg/kg) and irradiation. Both the vehicle and **KSL0608-Se** were administrated by intraperitoneal injection once every two weeks and for eight weeks. According to the *in-vivo* imaging results using **KSL0608-O**, the mice of "**KSL0608-Se** + irradiation" group were irradiated four times every two weeks after the administration of **KSL0608-Se**. All mice were sacrificed on 68 days. For imaging experiments *in vivo*, mice aged 2 months and 21 months (male, n = 3) were intraperitoneally injected with **KSL0608-O** (20 mg/kg), respectively.

Tissue sections and blood samples. Main organs of mice (heart, liver, spleen, lung and kidney) were isolated, washed with PBS, and transferred to liquid nitrogen. All these organs were paraffin-embedded with paraffin and sectioned into 5 μm slices for H&E staining. The frozen kidneys and livers were sliced at -20 °C and sectioned into 20-μm-thick sections using a cryocut microtome (CRYOSTAR NX50, Thermo) and mounted onto glass slides (Servicebio). The sections were stored at -20 °C and used in one day. Additionally, the blood samples of all mice were collected and stewed for 1 h at room temperature. Then, the blood samples were centrifuged (3000 g, 20 min) at 4 °C to obtain serum.

PDT and imaging *in vivo*. The PDT experiments were performed on *in vivo* fluorescence imaging system (Perkin Elmer IVIS Spectrum CT imaging system) with an excitation wavelength at 535 nm for 20 min. The hair on the back and abdomen of mice was shaved. Then, the mice were anaesthetized with isoflurane and were placed on the loading platform of instrument (3-4 mice at a time), followed by intermittent irradiation using sequence imaging mode (Excitation filter: 535; Subject size: 1.5; Field of view: 22.4). The mice with doxo-induced senescence were irradiated once a day for three consecutive days after the administration of **KSL0608-Se**. The naturally aged mice were irradiated once a day for four consecutive days after the administration of **KSL0608-Se**. The PDT treatment was performed on day 24, 25 and 26 for mice with doxo-induced senescence and was carried out on day 1, 2, 3, 4, 15, 16, 17, 18, 29, 30, 31, 32, 43, 44, 45 and 46 for naturally aged mice.

The imaging experiments in those mice were performed on *in vivo* fluorescence imaging system (Perkin Elmer IVIS Spectrum CT imaging system) (Ex: 535 nm, Em: 640-660 nm). The hair on the back and abdomen of mice was shaved. The images were taken on at 1 h, 12 h, 24 h, 72 h and 96 h after injection. Then, these mice were sacrificed and their major organs (heart, liver, spleen, lung

and kidney) were harvested and subjected to *ex vivo* imaging.

Western blot analysis. The prepared liver and kidney samples of mice were placed in grinders. Total protein was extracted using RIPA lysis buffer containing protease inhibitor. The concentration of protein was quantified by BCA protein assay kit (Yeasen). After mixing the SDS-PAGE protein loading buffer, the solution was heated at 100 ºC for 10 min. Then, samples with equal protein amount were added into the wells with 10% (or 12%) SDS-PAGE gel and were separated and transferred to a PVDF membrane. The membranes were then blocked and incubated with primary antibody (γ-H2AX: Abcam, ab81299, 1/10000 dilution; p21: Cell Signaling Technology, 2947S, 1/1000 dilution; p53: Santa Cruz, sc-126, 1/1000 dilution; GAPDH: Abclonal, ac033, 1/2000 dilution) at 4 °C overnight and then was washed with TBST for five times. After incubating with secondary antibodies (Anti-rabbit IgG antibody, CST, 7074P2; Goat anti-Mouse IgG antibody, Arigo, ARG65350) for 1 h, the membranes were imaged using an imaging system (Tanon-4600SF).

Reverse transcription (RT)-quantitative PCR (RT-qPCR). The prepared liver and kidney samples of mice were placed in grinders. Total RNA was extracted using RNA Isolation Kit (Omega, Biotek) according to the manufacturer's instructions. cDNA was generated by using Hifair II 1st strand cDNA synthesis supermax for qPCR (gDNA digester plus) (Yesen). RT–qPCR was performed using Hieff UNICON® Universal Blue qPCR SYBR Green Master Mix (Yesen) on a qPCR detecting system (BIO-RAD, CFX96) by following the manufacturer's instructions.
Four biological repeats were conducted for each group. The test procedure was in accordance with the instruction of kit. GAPDH was used as a control to normalize the expression of target genes. The primers (Sangon Biotech) used are listed as follows:
GADPH, forward: GTGGCAAAGTGGAGATTGTTG;
reverse: AGTCTTCTGGGTGGCAGTGAT.
p21, forward: CAGATCCACAGCGATATCCA;
reverse: ACGGGACCGAAGAGACAAC.
IL-1β, forward: TGCCACCTTTTGACAGTGATG;
reverse: TGATGTGCTGCTGCGAGATT.

Immunofluorescence staining. Kidney and liver samples for immunofluorescence staining assays were incubated with primary antibody (p21: Cell Signaling Technology, 2947S, 1/200) at 4 ºC overnight, washed three times with PBS and then incubated with appropriate secondary antibodies (Anti-rabbit IgG antibody, CST, 7074P2, 1/500) for 1 h at 37 °C. And then the samples were stained by Hoechst.

ELISA analysis. SASP factors (IL-6、IL-1β、CXCL1、CXCL3、MMP-1、MMP-7 and TNF-α), and cell cycle regulators p16 (CDKN2A) in serum, liver or kidney were monitored using ELISA Kit (RF6857, RF7630, RF8477, RF7606, RF7480, RF7678, RF7722, RF6978). AST, ALT, UA, Cr and BUN in serum were teste using ELISA Kit (RF8502, RF8547, RF8520, RF8275, RF8274). All ELISA Kits were purchased in Shanghai ruifan Biological Technology Co, Ltd. And the data of ELISA analysis were collected by this company.

Physical function measurements. All functional assays were conducted one week before the sacrifice of mice.

The rotarod test was performed using an accelerating RotaRod system (Shanghai XinRuan Information Technology Co., Ltd, XR-6C). Mice were placed in separate lanes on the rod rotating at an initial speed of 4 rpm/min and then the speed accelerated from 4 to 40 rpm/min in 300 s. The time, speed and distance were recorded when the mouse fell to the bottom of machine. All mice were trained once a day for three consecutive days (day 1, 2 and 3) and the test were recorded on day 4, 5 and 6. The results were averaged from 3 trials.

The grip strength of mice was measured by a grid strength meter (Shanghai XinRuan Information Technology Co., Ltd, XR501). Mice were placed in the grid of the machine and grasped the grid with all four paws. The meter recorded the peak tension over six trials. The test was performed once a day for three consecutive days and the results were averaged from 3 trials.

For the Y-maze spontaneous-alternation test, the mice were placed in the centre of a Y-shaped maze (XinRuan Information Technology Co., Ltd, XR-XY1032). The mice are allowed to explore all three arms freely. The number of arm entries and sequences of arm visits of mice within 8 min were recorded and analyzed.

To perform the hanging test, mice were kept to grab a 2-mm-thick metal wire (35 cm above a padded surface) with their forelimbs only and recorded the hanging duration. Hanging time was normalized to body weight as hanging duration (sec) × body weight (g), and the results were averaged from 3 trials for each mouse.

RNA sequencing. For the PDT experiments on doxo-treated mice and naturally aged mice, the liver samples of mice in different groups were collected for RNA sequencing in Shanghai Majorbio Bio-pharm Technology Co., Ltd. Data was analyzed using the free online platform of Majorbio Cloud Platform. The accession number for RNA-seq reported in this paper is GEO: GSE186522 and GSE213846.

Statistics and reproducibility. Leica Application Suite X and ImageJ 1.49k were used to process imaging data. Graphpad Prism

6.01, OriginPro 8.0 and CytExpert 2.4 were used for data analysis. Statistical analyses were performed in GraphPad Prism 6.01 with the Student's t-test and one-way ANOVA. Statistical significance is represented in the figures. For *in vivo* studies, mice were randomly assigned to treatment groups. All replicates in this work represent different mice. The experiments were repeated independently at least twice with similar results. No sample sizes were pre-determined, but our sample sizes are similar to those reported in previous publications[9,11,26]. Blinding was not conducted and all data collection and analysis were objective in nature. No data were excluded from the analysis. Data distribution was assumed to be normal but this was not formally tested.

Reporting summary. Further information on research design is available in the Nature Research Reporting Summary linked to this article.

Data availability

All data during the current study are available within the paper and its Supplementary Information, or from the corresponding author upon reasonable request.

Code availability

Source code used for RNA-seq analysis can be found at https://www.ncbi.nlm.nih.gov/geo/query/acc.cgi?acc=GSE186522. https://www.ncbi.nlm.nih.gov/geo/query/acc.cgi?acc=GSE213846.

References

1. Pan, C. & Locasale, J. Targeting metabolism to influence aging. *Science* **371**, 234-235 (2021).
2. Chen, Y. *et al.* Aging reprograms the hematopoietic- vascular niche to impede regeneration and promote fibrosis. *Cell Metab.* **33**, 395-410 (2021).
3. Chatsirisupachai, K., Palmer, D., Ferreira, S. & de Magalhaes, J. P. A human tissue-specific transcriptomic analysis reveals a complex relationship between aging, cancer, and cellular senescence. *Aging Cell* **18**, e13041 (2019).
4. Farr, J. N. *et al.* Targeting cellular senescence prevents age-related bone loss in mice. *Nat. Med.* **23**, 1072-1079 (2017).
5. Lee, J. S. *et al.* Pak2 kinase promotes cellular senescence and organismal aging. *Proc. Natl. Acad. Sci. U. S. A.* **116**, 13311-13319 (2019).
6. Takahashi, A. *et al.* Downregulation of cytoplasmic DNases is implicated in cytoplasmic DNA accumulation and SASP in senescent cells. *Nat. Commun.* **9**, 1249 (2018).
7. Baker, D. J. *et al.* Clearance of p16Ink4a-positive senescent cells delays ageing-associated disorders. *Nature* **479**, 232-236 (2011).
8. Chang, J. *et al.* Clearance of senescent cells by ABT263 rejuvenates aged hematopoietic stem cells in mice. *Nat. Med.* **22**, 78-83 (2016).
9. Cai, Y. *et al.* Elimination of senescent cells by β-galactosidase-targeted prodrug attenuates inflammation and restores physical function in aged mice. *Cell Res.* **30**, 574-589 (2020).
10. Guerrero, A. *et al.* Galactose-modified duocarmycin prodrugs as senolytics. *Aging Cell* **19**, e13133 (2020).
11. Novais, E. J. *et al.* Long-term treatment with senolytic drugs Dasatinib and Quercetin ameliorates age-dependent intervertebral disc degeneration in mice. *Nat. Commun.* **12**, 5213 (2021).
12. Suda, M. *et al.* Senolytic vaccination improves normal and pathological age-related phenotypes and increases lifespan in progeroid mice. *Nat. Aging* **1**, 1117-1126 (2021).
13. Xu, Q. *et al.* The flavonoid procyanidin C1 has senotherapeutic activity and increases lifespan in mice. *Nat. Metab.* **3**, 1706-1726 (2021).
14. Xu, M. *et al.* Senolytics improve physical function and increase lifespan in old age. *Nat. Med.* **24**, 1246-1256 (2018).
15. Micco, R. D. *et al.* Cellular senescence in ageing: from mechanisms to therapeutic opportunities. *Nat. Rev. Mol. Cell Biol.* **22**, 75-95 (2021).
16. Zhu, Y. *et al.* The Achilles' heel of senescent cells: from transcriptome to senolytic drugs. *Aging Cell* **14**, 644-658 (2015).
17. Hickson, L. J. *et al.* Senolytics decrease senescent cells in humans: Preliminary report from a clinical trial of Dasatinib plus Quercetin in individuals with diabetic kidney disease. *EBioMedicine* **47**, 446-456 (2019).
18. Pungsrinont, T. *et al.* Senolytic compounds control a distinct fate of androgen receptor agonist- and antagonist-induced cellular senescent LNCaP prostate cancer cells. *Cell Biosci.* **10**, 59 (2020).
19. Yosef, R. *et al.* Directed elimination of senescent cells by inhibition of BCL-W and BCL-XL. *Nat. Commun.* **7**, 11190 (2016).
20. Wendt, M. D. Discovery of ABT-263, a Bcl-family protein inhibitor: observations on targeting a large protein-protein interaction. *Expert Opin. Drug Discov.* **3**, 1123-1143 (2008).
21. Zhu, Y. *et al.* Identification of a novel senolytic agent, navitoclax, targeting the Bcl-2 family of anti-apoptotic factors. *Aging Cell* **15**, 428-435 (2016).
22. He, Y. et al. Using proteolysis-targeting chimera technology to reduce navitoclax platelet toxicity and improve its senolytic activity. *Nat. Commun.* **11**, 1996 (2020).
23. Yousefzadeh, M. J. *et al.* Fisetin is a senotherapeutic that extends health and lifespan. *EBioMedicine* **36**, 18-28 (2018).

24 Wang, Y. *et al.* Discovery of piperlongumine as a potential novel lead for the development of senolytic agents. *Aging-US* **8**, 2915-2926 (2016).
25 Menicacci, B. *et al.* Chronic resveratrol treatment inhibits MRC5 fibroblast SASP-related protumoral effects on melanoma Cells. *J. Gerontol. A Biol. Sci. Med. Sci.* **72**, 1187-1195 (2017).
26 Johmura, Y. *et al.* Senolysis by glutaminolysis inhibition ameliorates various age-associated disorders. *Science* **371**, 265-270 (2021).
27 Kirkland, J. L. & Tchkonia, T. Senolytic drugs: from discovery to translation. *J. Intern. Med.* **288**, 518-536 (2020).
28 Fuhrmann-Stroissnigg, H., Niedernhofer, L. J. & Robbins, P. D. Hsp90 inhibitors as senolytic drugs to extend healthy aging. *Cell Cycle* **17**, 1048-1055 (2018).
29 Wu, L., Liu, J., Li, P., Tang, B. & James, T. D. Two-photon small-molecule fluorescence-based agents for sensing, imaging, and therapy within biological systems. *Chem. Soc. Rev.* **50**, 702-734 (2021).
30 Zhai, W. *et al.* Universal scaffold for an activatable photosensitizer with completely inhibited photosensitivity. *Angew. Chem. Int. Ed. Engl.* **58**, 16601-16609 (2019).
31 Lu, M. *et al.* Mitochondria-targeting plasmonic spiky nanorods increase the elimination of aging cells in vivo. *Angew. Chem. Int. Ed. Engl.* **59**, 8698-8705 (2020).
32 Sun, J. *et al.* Cascade reactions by nitric oxide and hydrogen radical for anti-hypoxia photodynamic therapy using an activatable photosensitizer. *J. Am. Chem. Soc.* **143**, 868-878 (2021).
33 Gao, Y. *et al.* Two-dimensional design strategy to construct smart fluorescent probes for the precise tracking of senescence. *Angew. Chem. Int. Ed. Engl.* **60**, 10756-10765 (2021).
34 Gnaim, S. *et al.* Direct real-time monitoring of prodrug activation by chemiluminescence. *Angew. Chem. Int. Ed. Engl.* **57**, 9033-9037 (2018).
35 Li, M. Y. *et al.* Mitochondria-immobilized fluorescent probe for the detection of hypochlorite in living cells, tissues, and zebrafishes. *Anal. Chem.* **92**, 3262-3269 (2020).
36 Doura, T. *et al.* Detection of lacZ-positive cells in living tissue with single-cell resolution. *Angew. Chem. Int. Ed. Engl.* **55**, 9620-9624 (2016).
37 Liu, J. *et al.* Bioorthogonal coordination polymer nanoparticles with aggregation-induced emission for deep tumor-penetrating radio- and radiodynamic therapy. *Adv. Mater.* **33**, e2007888 (2021).
38 Lim, G. T. *et al.* Bioorthogonally surface-edited extracellular vesicles based on metabolic glycoengineering for CD44-mediated targeting of inflammatory diseases. *J. Extracell Vesicles* **10**, e12077 (2021).
39 Chang, T. C., Vong, K., Yamamoto, T. & Tanaka, K. prodrug activation by gold artificial metalloenzyme- catalyzed synthesis of phenanthridinium derivatives via hydroamination. *Angew. Chem. Int. Ed. Engl.* **60**, 12446-12454 (2021).
40 Bakkum, T. *et al.* Bioorthogonal correlative light-electron microscopy of mycobacterium tuberculosis in macrophages reveals the effect of antituberculosis drugs on subcellular bacterial distribution. *ACS Cent. Sci.* **6**, 1997-2007 (2020).
41 Benson, S. *et al.* Photoactivatable metabolic warheads enable precise and safe ablation of target cells in vivo. *Nat. Commun.* **12**, 2369 (2021).
42 Chiba, M. *et al.* An activatable photosensitizer targeted to gamma-glutamyltranspeptidase. *Angew. Chem. Int. Ed. Engl.* **56**, 10418-10422 (2017).
43 Graceffa, P. Spin labeling of protein sulfhydryl groups by spin trapping a sulfur radical: Application to bovine serum albumin and myosin. *Arch. Biochem. Biophys.* **225**, 802-808 (1983).
44 Xiong, T. *et al.* A singlet oxygen self-reporting photosensitizer for cancer phototherapy. *Chem. Sci.* **12**, 2515-2520 (2020).
45 Li, M. *et al.* Smart J-aggregate of cyanine photosensitizer with the ability to target tumor and enhance photodynamic therapy efficacy. *Biomaterials* **269**, 120532 (2021).
46 Won, M. *et al.* An ethacrynic acid-brominated BODIPY photosensitizer (EA-BPS) construct enhances the lethality of reactive oxygen species in hypoxic tumor-targeted photodynamic therapy. *Angew. Chem. Int. Ed. Engl.* **60**, 3196-3204 (2021).
47 Sun, J. *et al.* GSH and H_2O_2 co-activatable mitochondria-targeted photodynamic therapy under normoxia and hypoxia. *Angew. Chem. Int. Ed. Engl.* **59**, 12122-12128 (2020).
48 Bartesaghi, A. *et al.* 2.2 A resolution cryo-EM structure of β-galactosidase in complex with a cell-permeant inhibitor. *Science* **348**, 1147-1151 (2015).
49 Chai, X. *et al.* Photochromic fluorescent probe strategy for the super-resolution imaging of biologically important biomarkers. *J. Am. Chem. Soc.* **142**, 18005-18013 (2020).
50 Bursuker, I., Rhodes, J. M., Goldman R. β-galactosidase-an indicator of the maturational stage of mouse and human mononuclear phagocytes. *J. Cell. Physiol.* **112**, 385-390 (1982).
51 Gaikwad, S. M. et al. A small molecule stabilizer of the MYC G4-quadruplex induces endoplasmic reticulum stress, senescence and pyroptosis in multiple myeloma. *Cancers (Basel)* **12**, 2952 (2020).
52 Mostoslavsky, R. et al. Genomic instability and aging-like phenotype in the absence of mammalian SIRT6. *Cell* **124**, 315-329 (2006).
53 Baar, M. P. *et al.* Targeted apoptosis of senescent cells restores tissue homeostasis in response to chemotoxicity and aging. *Cell* **169**, 132-147 e116 (2017).
54 Kong, S. Z. *et al.* Anti-aging effect of chitosan oligosaccharide on d-galactose-induced subacute aging in mice. *Mar. Drugs* **16**,

181 (2018).
55 Wang, Y. *et al.* The role of IL-1β and TNF-α in intervertebral disc degeneration. *Biomed. Pharmacother.* **131**, 110660 (2020).
56 Parker, C. A. & Rees, W. T. Correction of fluorescence spectra and measurement of fluorescence quantum efficiency. *Analyst* **85**, 587-600 (1960).
57 Zhai, W. *et al.* Universal scaffold for an activatable photosensitizer with completely inhibited photosensitivity. *Angew. Chem. Int. Ed. Engl.* **58**, 16601-16609 (2019).
58 Redmond, R. W. & Gamlin, J. N. A compilation of singlet oxygen yields from biologically relevant molecules. *Photochem. Photobiol.* **70**, 391-475 (1999).
59 He, L. *et al.* Global characterization of macrophage polarization mechanisms and identification of M2-type polarization inhibitors. *Cell Rep*. **37**, 109955 (2021).
60 Yang, W. et al. Role of Azole Drugs in Promoting Fungal Cell Autophagy Revealed by an NIR Fluorescence-Based Theranostic Probe. *Anal. Chem.* **94**, 7092-7099 (2022).
61 Liu, Y. *et al.* A Cyanine Dye to Probe Mitophagy: Simultaneous Detection of Mitochondria and Autolysosomes in Live Cells. *J. Am. Chem. Soc.* **138**, 12368-12374 (2016).
62 Jannone, G., Rozzi, M., Najimi, M., Decottignies, A. & Sokal, E. M. An optimized protocol for histochemical detection of senescence-associated beta-galactosidase activity in cryopreserved liver tissue. *J. Histochem. Cytochem.* **68**, 269-278 (2020).

Acknowledgements

We gratefully appreciate the financial support from the National Natural Science Foundation of China (Grants 22037002 to J.L. and Yuan Guo, 32121005 to J.L., 21977082 to Yuan Guo and 22007032 to Xinming Li), the Natural Science Basic Research Program of Shaanxi (Grant 2020JC-38 to Yuan Guo), the Innovation Program of Shanghai Municipal Education Commission (Grant 2021-01-07-00-02-E00104 to J.L.), the Shanghai Frontier Science Research Base of Optogenetic Techniques for Cell Metabolism (Grant 2021 Sci & Tech 03-28 to J.L.), the Innovative Research Team of High-level Local Universities in Shanghai (Grant SHSMU-ZDCX20212702 to J.L.) and the Chinese Special Fund for State Key Laboratory of Bioreactor Engineering (2060204 to J.L.). T.D.J. wishes to thank the Royal Society for a Wolfson Research Merit Award and the Open Research Fund of the School of Chemistry and Chemical Engineering, Henan Normal University for support (Grant 2020ZD01 to T.D.J.). The funders had no role in study design, data collection and analysis, decision to publish or preparation of the manuscript.

Author contributions

Yuan Guo and J.L. conceived and designed the project. Yuan Guo, J.L., D.S., Ying Gao and T.D.J. wrote and revised the manuscript. D.S. and Xinming Li performed the synthetic work. D.S. and W.L. performed and analyzed the experiments. Y.H. performed modelling assay. Xiaokang Li assisted with data analysis.

Competing interests

The authors declare no competing financial interests.

Figure Legends

Figs. 1-8

Fig. 1 | Integrated design strategy. a, Synthetic routes of **KSL0608-O** and **KSL0608-Se**. **b**, Integrated strategy used to design the senotherapeutic agent **KSL0608-Se**.

Fig. 2 | Photochemical properties and β-gal-triggered protein labelling. a,**b**, The normalized fluorescence intensity of **KSL0608-O** (10 μM, **a**) and **KSL0608-Se** (10 μM, **b**) in the presence and absence of *E. coli* β-gal (10 U/mL) and BSA (1 mg/mL). **c**, SDS-PAGE analysis of **KSL0608-O** (10 μM) and **KSL0608-Se** (10 μM) in the presence and absence of *E. coli* β-gal (10 U/mL) and BSA (1 mg/mL). **d**,**e**, Fluorescence spectra of **KSL0608-O** (10 μM, **d**) and **KSL0608-Se** (10 μM, **e**) upon the addition of different concentrations of *E. coli* β-gal at 37 °C in PBS buffer containing BSA (1 mg/mL). **f**, Schematic diagram of human-β-gal-**KSL0608-O** interactions (PDB: 3THC). **g**, Electrostatic surface potential of the substrate-binding pocket in human β-gal with galactose and **KSL0608-O**. **h**, Normalized absorption spectra of DPBF in different groups. **i**, Normalized absorption spectra of DPBF in a solution with **KSL0608-Se**, *E. coli* β-gal (4 U/mL) and BSA (1 mg/mL) under light irradiation (535 nm, 10 mW/cm^2). Error bars (**a**, **b**, and **h**) represent the standard deviation (± S.D.). n = 3 independent samples.

Fig. 3 | Cell imaging and intracellular localization of KSL0608-O and KSL0608-Se. a, X-gal staining of young cells and SnCs for β-gal expression (Scale bar: 200 μm) and confocal fluorescence images of **KSL0608-O** and **KSL0608-Se** in different cells (Scale bar: 50 μm), including young A549 cells, MitoC-induced senescent A549 cells, young HL-7702 cells, doxo-induced senescent HL-7702 cells, young NRK-52E cells, ROS-induced senescent NRK-52E cells, MRC-5 cells (P28) and MRC-5 cells (P40). A549 cells, HL-7702 cells and NRK-52E cells were incubated **KSL0608-Se** (10 μM) for 30 min, respectively. MRC-5 cells were incubated with **KSL0608-Se** (5 μM) for 30 min; All these cells were incubated with **KSL0608-O** (10 μM) for 30 min. **b**,**c**, Normalized fluorescence intensity of the cells incubated with **KSL0608-O** and **KSL0608-Se** from parallel images including (**a**). (**b**: n = 10 for A549 cells, n = 11 for NRK-52E cells, n = 9 for HL-7702 cells and n = 6 for MRC-5 cells; **c**: n = 10 for A549 cells, n = 10 for NRK-52E cells, n = 9 for HL-7702 cells and n = 7 for MRC-5 cells). Error bars represent the standard deviation (± S.D.). The significance of differences was analyzed with two-sided Student's t-test. **c**, Confocal fluorescence images showing the subcellular localization of **KSL0608-O** (10 μM) and **KSL0608-Se** (10 μM) in replication-induced senescent MRC-5 cells (P40). All cells were stained with Hoechst33258 (Hoechst, 1 μM). Column 3 and column 6 represent cross-sectional analyses along the white lines in the insets. Scale bar: 25 μm. Abbreviations: yng, young; sct, senescent. Blue channel: $\lambda_{ex}/\lambda_{em}$ = 405/420−440 nm. Green channel: $\lambda_{ex}/\lambda_{em}$ = 488/500-530 nm. NIR channel (**KSL0608-O**): $\lambda_{ex}/\lambda_{em}$ = 561/600−700 nm. NIR channel (**KSL0608-Se**): $\lambda_{ex}/\lambda_{em}$ = 561/650−750 nm. 'n' stands for the number of image and the images in each group from three biological replicates.

Fig. 4 | Photo-induced ROS generation and PDT effect *in vitro*. a, Fluorescence image of intracellular ROS stained by 2,7-dichlorofluorescein diacetate (DCFH-DA, 10 μM) in SKOV3 cells incubated with **KSL0608-Se** (10 μM) before and after irradiation (n = 10). Scale bar: 50 μm. **b**, Live/dead cell assays of SKOV3 cells in different groups using calcein-AM and propidium iodide (PI). Scale bar: 100 μm. **c**, Cytotoxicity assay of **KSL0608-Se**-mediated PDT to different cells, including young A549 cells, young HL-7702 cells, young NRK-52E cells and MRC-5 cells (P28), MitoC-induced senescent A549 cells, doxo-induced senescent HL-7702 cells, ROS-induced senescent NRK-52E cells and MRC-5 cells (P40) (n = 3 for each group). **d**,**e**, Flow cytometric plots to measure apoptosis (**d**) and quantitate the percentage of apoptotic cells, surviving cells and necrotic cells (**e**) in **KSL0608-Se** (10 μM)-loaded cells (MRC-5 cells (P28) and MRC-5 cells (P40)) treated with or without irradiation. **f**,**g**, Real-time confocal imaging of cells in co-cultured systems incubated with 10 μM **KSL0608-O** (**f**) and 10 μM **KSL0608-Se** (**g**) after irradiation. Young cells were pre-labelled by CellTracker Green (5 μM), and all cells were pre-stained by Hoechst (1 μM). The co-cultured cells were incubated with our compound for 30 min at 37 °C and then treated with laser irradiation at 561 nm. Scale bar: 50 μm. Error bars (**a** and **c**) represent the

standard deviation (± S.D.). Significant differences were analyzed with the two-sided Student's t-test. 'n' stands for the number of image and the images in each group from three biological replicates.

Fig. 5 | Fluorescence imaging using KSL0608-O *in vivo*. **a**, Representative whole-body imaging in young mice (2-month-old) and naturally aged mice (21-month-old) at different times after injection of **KSL0608-O**. **b**, Quantitative analysis of the fluorescence imaging of mice from parallel images including (**a**). **c**, Representative images of *ex vivo* imaging of five major organs (heart, liver, spleen, lung and kidney) harvested from young mice (2-month-old) and naturally aged mice (21-month-old) at 96 h after injection of the **KSL0608-O**. **d**, Quantitative analysis of the fluorescence imaging of major organs from parallel images including (**c**). Error bars (**b** and **d**) represent the standard deviation (± S.D.). n = 3 for each group and 'n' stands for the number of mice

Fig. 6 | Selective removal of SnCs in doxo-treated mice. **a**, Experimental design of **KSL0608-Se**-mediated PDT in doxo-treated mice. **b**, Western blot analysis of γ-H2AX expression levels in kidneys and livers of mice in different groups (n = 3 for each group). The samples derive from the same experiment and that gels/blots were processed in parallel. **c**, The serum biochemical test of AST (left) and ALT (right) in different groups (n = 4 for each group). **d**, The relative mRNA levels of *p21* in livers (left) and kidneys (right) of mice in different groups (n = 4 for each group) analyzed by RT-qPCR. **e**, Representative images of SA-β-gal staining (X-gal and **KSL0608-O**) of kidney sections of mice in different groups. NIR channel (**KSL0608-O**): $\lambda_{ex}/\lambda_{em}$ = 561/600−700 nm. Scale bar: 100 μm. **f**, A volcano plot of gene expression in doxo control group compared to young control group (left), and a volcano plot of gene expression in **KSL0608-Se** + irradiation group compared to doxo control group (right) (more than twofold, $P < 0.05$, calculated by raw count value). **g**, Venn diagram showing the number of differential genes and overlapped genes between A and B (A, doxo control group vs. young control group; B, **KSL0608-Se** + irradiation group vs. doxo control group). **h**, Heatmap of senescence-related genes of livers in different groups, where '#' represents no significance genes in livers of all mice. n = 4 for each group in RNA sequencing analysis. Error bars (**b**-**d**) represent the standard deviation (± S.D.). 'n' stands for the number of mice. Significant differences (**b**-**d**) were obtained by analysis with two-sided Student's t-test.

Fig. 7 | Selective removal of SnCs in naturally aged mice. **a**, Experimental design of **KSL0608-Se**-mediated PDT in naturally aged mice. **b**, Western blot analysis of p53 expression levels in kidneys and livers of mice in different groups (n = 3 for each group). The samples derive from the same experiment and that gels/blots were processed in parallel. **c**, Representative images of SA-β-gal staining of livers sections and kidney sections, and the percentage of SA-β-gal-positive area in these sections from mice in different groups (young control, n = 10; aged control, n = 8; **KSL0608-Se**, n = 11; **KSL0608-Se** + irradiation, n = 11). Scale bar: 100 μm. **d**, Representative images of p21 IF staining of kidney sections and liver sections, and the p21 expression levels in these sections from mice in different groups (n = 6 for each group). Scale bar: 100 μm. **e**, The serum biochemical test of UA (left), Cr (middle) and BUN (right) from mice in different groups. **f**, The serum biochemical test of ALT (left) and AST (right) from mice in different groups. For **e**,**f**, young control, n = 12; aged control, n = 9; **KSL0608-Se**, n = 11; **KSL0608-Se** + irradiation, n = 11. Error bars (**b-f**) represent as the mean values (± S.D.). 'n' stands for the number of mice. Significant differences (**b-f**) were obtained by analysis with two-sided Student's t-test (**b-d**) and one-way ANOVA followed by Tukey's multiple comparisons test (**e,f**).

Fig. 8 | The expression of SASP factors, evaluation of physical function in mice and RNA sequencing analysis. **a-g**, The expression levels of CXCL1 (**a**), CXCL3 (**b**), IL-1β (**c**), IL-6 (**d**), MMP-1 (**e**), MMP-7 (**f**) and TNF-α (**g**) in blood serum of mice in different groups (young control, n = 12; aged control, n = 9; **KSL0608-Se**, n = 11; **KSL0608-Se** + irradiation, n = 11). **h**, Quantification of the ratio of grip strength to weight from mice in different groups. **i**, Quantification of maximal time in rotarod from mice in different groups. **j**, Quantification of hanging endurance from mice in different groups. **k**, The alteration (left) and total arm entries (right) in a Y-maze test from mice in different groups. For **h-k**, young control, n = 12; aged control, n = 9; **KSL0608-Se**, n = 11; **KSL0608-Se** + irradiation, n = 10. Error bars (**a-k**) represent as the mean values (± S.D.). Significant differences (**a-k**) (ns, not significant) were obtained by analysis with one-way ANOVA followed by Tukey's multiple comparisons test (**a-g**) and two-sided Student's t-test (**h-k**). **l**, Venn diagram showing the number of differential genes and overlapped genes between A and B (A, aged control group vs. young control group; B, **KSL0608-Se** + irradiation group vs. aged control group). And the representative GO processes

770 associated with the 146 common differentially expressed genes. **m**,**n**, A volcano plot of gene expression in the aged
771 control group compared to the young control group (**m**), and that in the **KSL0608-Se** + irradiation group compared to the
772 aged control group (**n**) (more than twofold, $P < 0.05$, calculated by raw count value). **o**, Heatmap of age-related genes of
773 livers in different groups, where '#' represents no significance genes in livers of all mice. n = 5 for each group in RNA
774 sequencing analysis. 'n' stands for the number of mice.
775

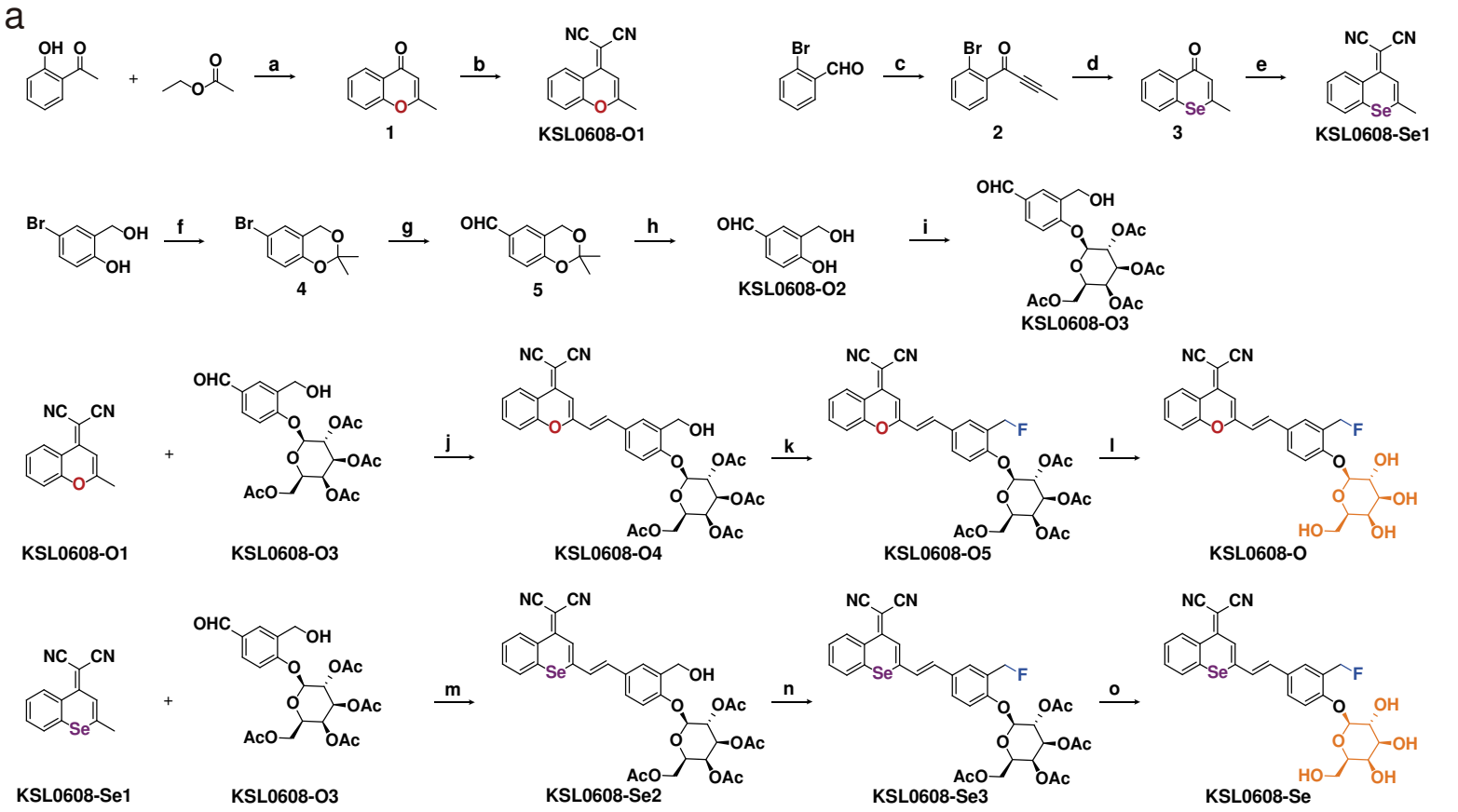

Reagents and conditions: a: NaH, H_2SO_4/CH_3COOH, r.t.; b: Malononitrile, Ac_2O, 140 °C; c: $CH_3CCMgBr$, THF; NaOCl, TEMPO, $NaHCO_3$, DCM; d: $NaBH_4$, Se, DMF, 100 °C; e: Malononitrile, Ac_2O, 140°C; f: Acetone, 2,2-dimethoxypropane, *p*-TsOH, Na_2SO_4, 40 °C; g: THF, *n*-BuLi, DMF, -78 °C; h: CH_3CN/H_2O, (cat.) HCl; i: K_2CO_3, DMF, tetra-O-acetyl-α-D-galactopyranosyl-1-bromide, r.t.; j: Piperidine, CH_3CN, 85 °C; k: DAST, DCM, 0 °C; l: MeOH, MeONa, r.t.; m: Piperidine, CH_3CN, 85 °C; n: DAST, DCM, 0 °C; o: MeOH, MeONa, r.t..

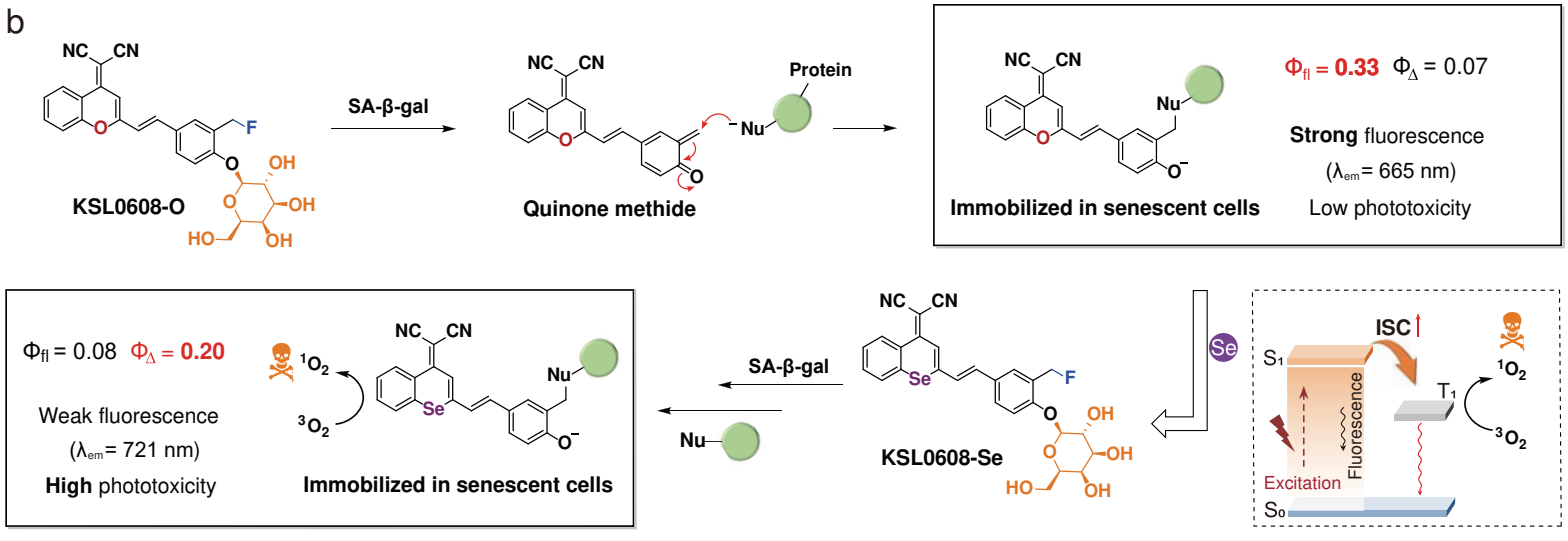

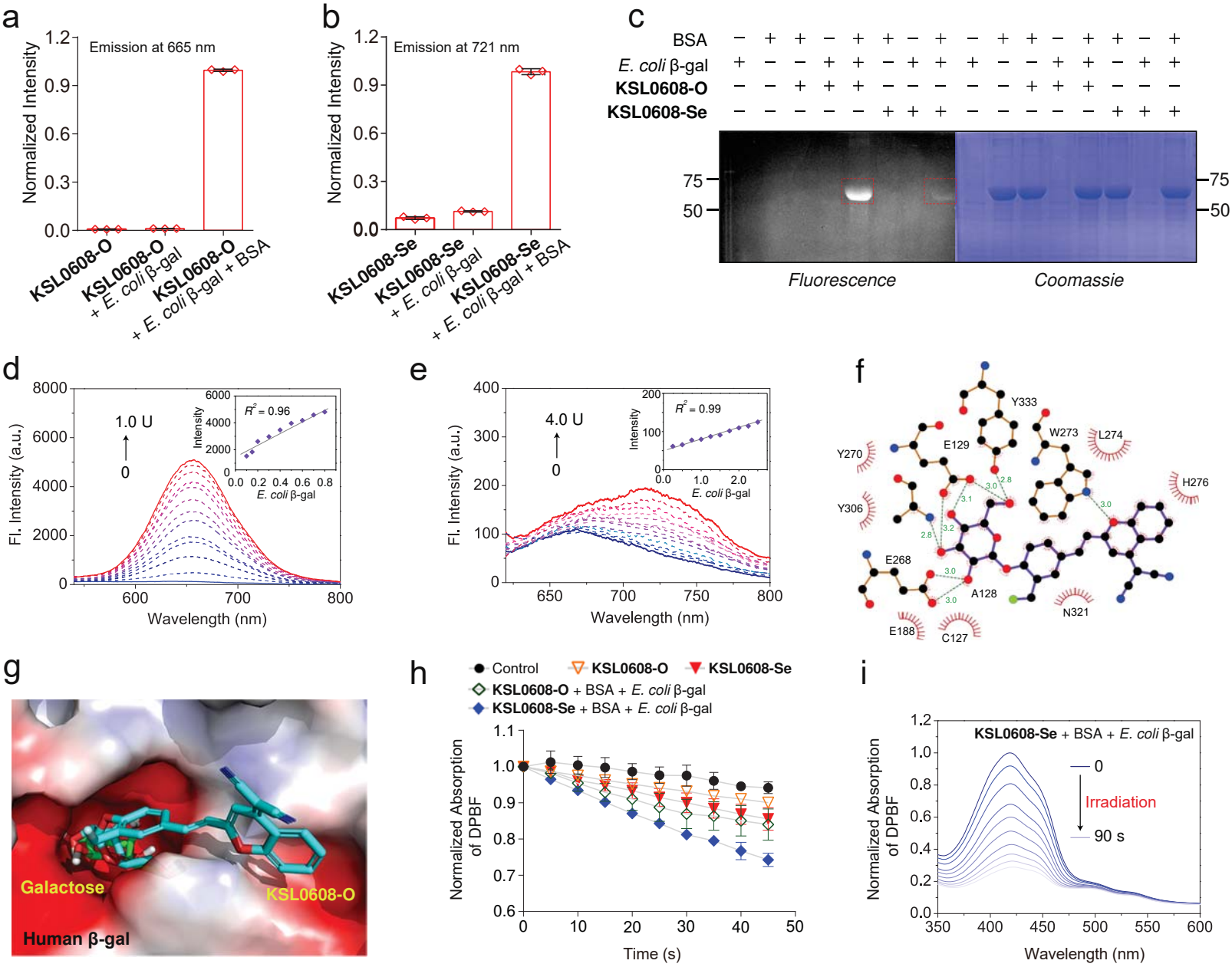
a
Emission at 665 nm
Normalized Intensity
KSL0608-O
KSL0608-O + E. coli β-gal
KSL0608-O + E. coli β-gal + BSA
b
Emission at 721 nm
Normalized Intensity
KSL0608-Se
KSL0608-Se + E. coli β-gal
KSL0608-Se + E. coli β-gal + BSA
c
BSA
E. coli β-gal
KSL0608-O
KSL0608-Se
75
50
Fluorescence
Coomassie
d
1.0 U
0
Fl. Intensity (a.u.)
Wavelength (nm)
R² = 0.96
Intensity
E. coli β-gal
e
4.0 U
0
Fl. Intensity (a.u.)
Wavelength (nm)
R² = 0.99
Intensity
E. coli β-gal
f
Y333
E129
W273
L274
Y270
H276
Y306
E268
A128
N321
E188
C127
g
Galactose
KSL0608-O
Human β-gal
h
Control
KSL0608-O
KSL0608-Se
KSL0608-O + BSA + E. coli β-gal
KSL0608-Se + BSA + E. coli β-gal
Normalized Absorption of DPBF
Time (s)
i
KSL0608-Se + BSA + E. coli β-gal
0
Irradiation
90 s
Normalized Absorption of DPBF
Wavelength (nm)

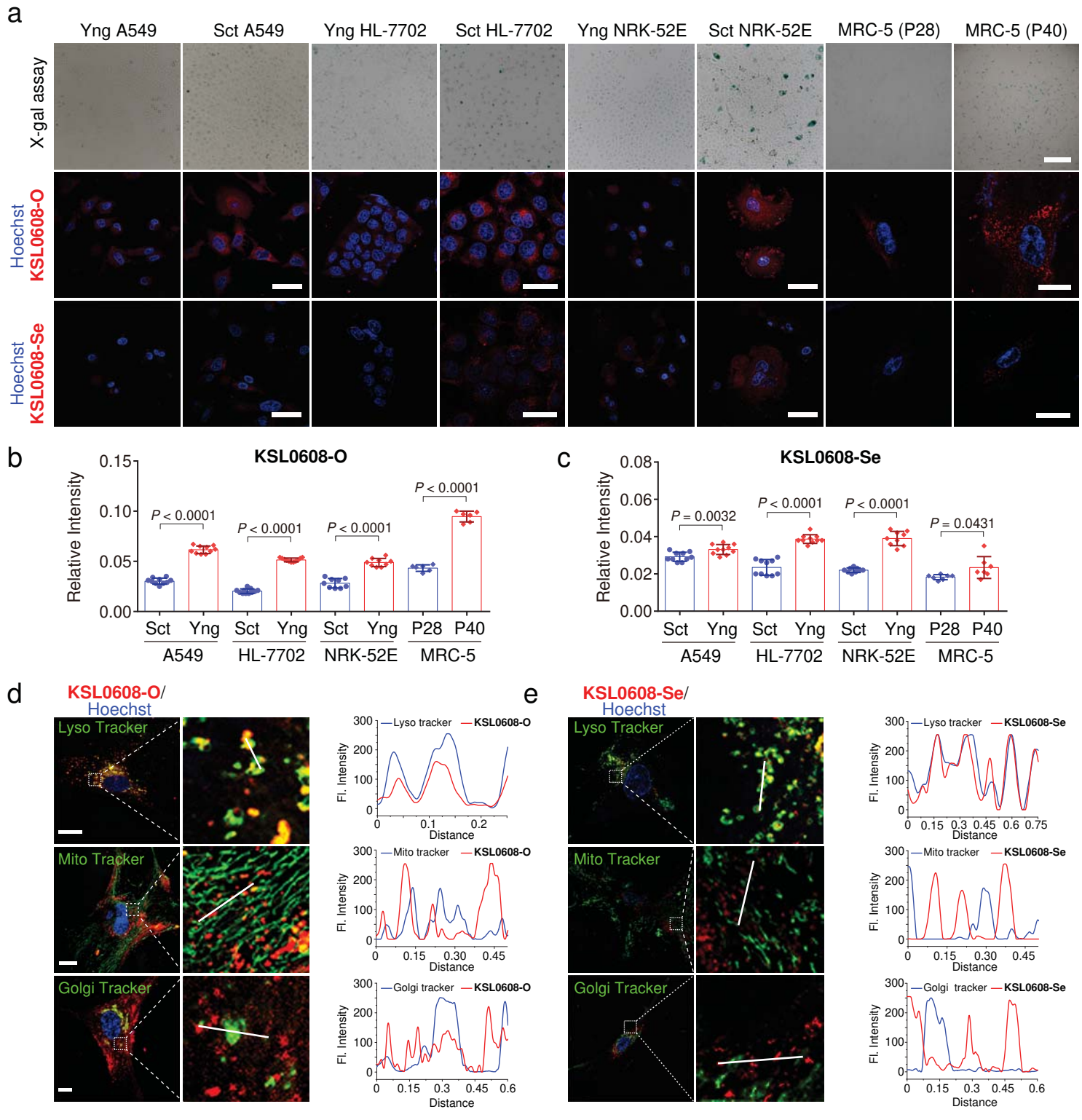
a
Yng A549
Sct A549
Yng HL-7702
Sct HL-7702
Yng NRK-52E
Sct NRK-52E
MRC-5 (P28)
MRC-5 (P40)
X-gal assay
Hoechst
KSL0608-O
Hoechst
KSL0608-Se
b
KSL0608-O
Relative Intensity
0.15
0.10
0.05
0.00
P < 0.0001
P < 0.0001
P < 0.0001
P < 0.0001
Sct
Yng
Sct
Yng
Sct
Yng
P28
P40
A549
HL-7702
NRK-52E
MRC-5
c
KSL0608-Se
Relative Intensity
0.08
0.06
0.04
0.02
0.00
P = 0.0032
P < 0.0001
P < 0.0001
P = 0.0431
Sct
Yng
Sct
Yng
Sct
Yng
P28
P40
A549
HL-7702
NRK-52E
MRC-5
d
KSL0608-O/
Hoechst
Lyso Tracker
Mito Tracker
Golgi Tracker
Fl. Intensity
Distance
Lyso tracker
KSL0608-O
Mito tracker
KSL0608-O
Golgi tracker
KSL0608-O
e
KSL0608-Se/
Hoechst
Lyso Tracker
Mito Tracker
Golgi Tracker
Fl. Intensity
Distance
Lyso tracker
KSL0608-Se
Mito tracker
KSL0608-Se
Golgi tracker
KSL0608-Se

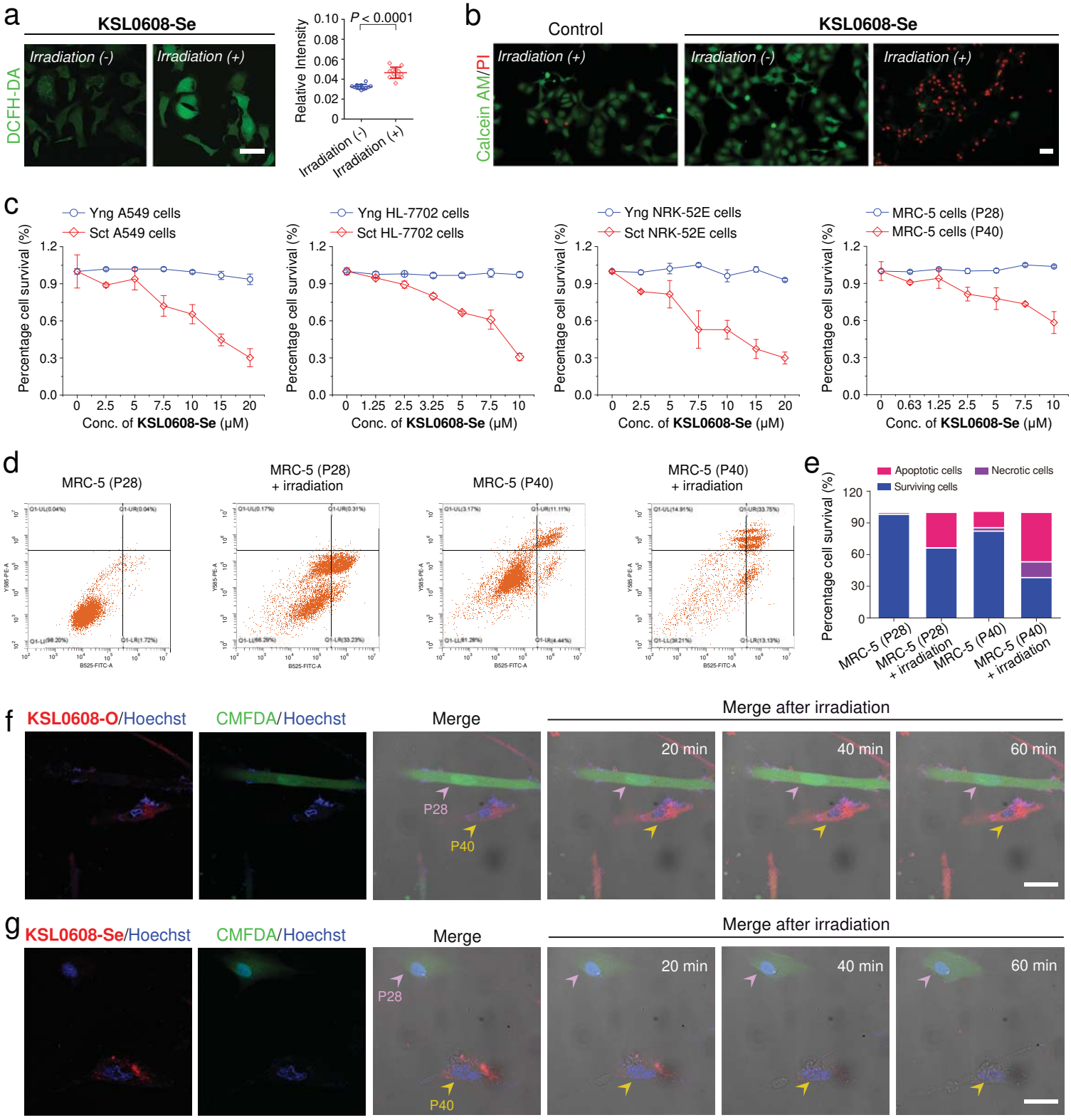
a
KSL0608-Se
DCFH-DA
Irradiation (-)
Irradiation (+)
Relative Intensity
P < 0.0001
Irradiation (-)
Irradiation (+)
b
Control
KSL0608-Se
Calcein AM/PI
Irradiation (+)
Irradiation (-)
Irradiation (+)
c
Yng A549 cells
Sct A549 cells
Yng HL-7702 cells
Sct HL-7702 cells
Yng NRK-52E cells
Sct NRK-52E cells
MRC-5 cells (P28)
MRC-5 cells (P40)
Percentage cell survival (%)
Conc. of KSL0608-Se (μM)
d
MRC-5 (P28)
MRC-5 (P28) + irradiation
MRC-5 (P40)
MRC-5 (P40) + irradiation
e
Apoptotic cells
Necrotic cells
Surviving cells
Percentage cell survival (%)
MRC-5 (P28)
MRC-5 (P28) + irradiation
MRC-5 (P40)
MRC-5 (P40) + irradiation
f
KSL0608-O/Hoechst
CMFDA/Hoechst
Merge
Merge after irradiation
20 min
40 min
60 min
P28
P40
g
KSL0608-Se/Hoechst
CMFDA/Hoechst
Merge
Merge after irradiation
20 min
40 min
60 min
P28
P40

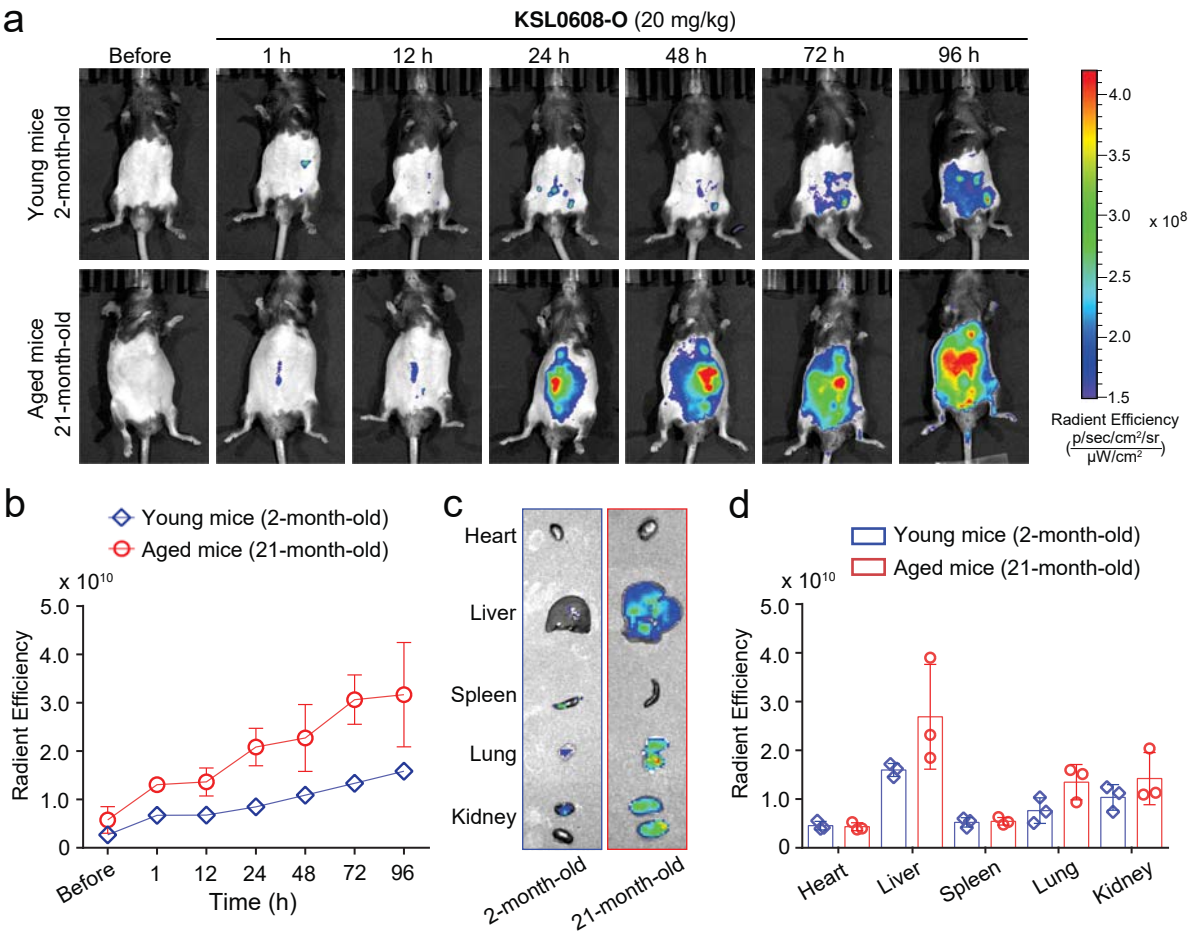
a
KSL0608-O (20 mg/kg)
Before
1 h
12 h
24 h
48 h
72 h
96 h
Young mice 2-month-old
Aged mice 21-month-old
4.0
3.5
3.0
2.5
2.0
1.5
x 10^8
Radient Efficiency
(p/sec/cm²/sr / μW/cm²)
b
Young mice (2-month-old)
Aged mice (21-month-old)
x 10^10
Radient Efficiency
5.0
4.0
3.0
2.0
1.0
0
Before
1
12
24
48
72
96
Time (h)
c
Heart
Liver
Spleen
Lung
Kidney
2-month-old
21-month-old
d
Young mice (2-month-old)
Aged mice (21-month-old)
x 10^10
Radient Efficiency
5.0
4.0
3.0
2.0
1.0
0
Heart
Liver
Spleen
Lung
Kidney

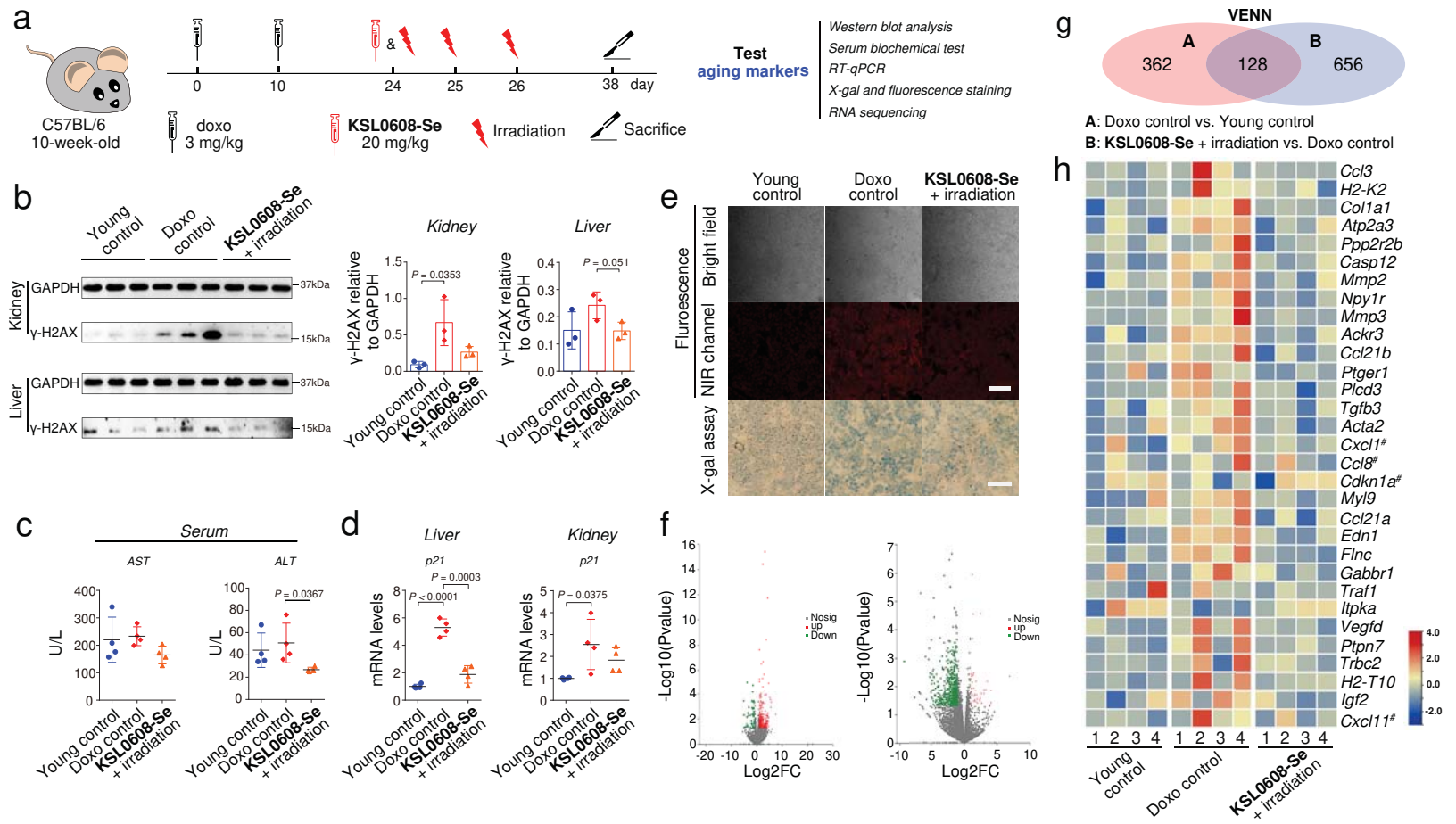
a
C57BL/6
10-week-old
0
10
24
25
26
38 day
doxo
3 mg/kg
KSL0608-Se
20 mg/kg
Irradiation
Sacrifice
Test
aging markers
Western blot analysis
Serum biochemical test
RT-qPCR
X-gal and fluorescence staining
RNA sequencing
b
Young control
Doxo control
KSL0608-Se + irradiation
Kidney
GAPDH
γ-H2AX
37kDa
15kDa
Liver
γ-H2AX relative to GAPDH
P = 0.0353
P = 0.051
c
Serum
AST
ALT
U/L
P = 0.0367
d
Liver
Kidney
p21
mRNA levels
P < 0.0001
P = 0.0003
P = 0.0375
e
Fluorescence
Bright field
NIR channel
X-gal assay
f
-Log10(Pvalue)
Log2FC
Nosig
Up
Down
g
VENN
A
B
362
128
656
A: Doxo control vs. Young control
B: KSL0608-Se + irradiation vs. Doxo control
h
Ccl3
H2-K2
Col1a1
Atp2a3
Ppp2r2b
Casp12
Mmp2
Npy1r
Mmp3
Ackr3
Ccl21b
Ptger1
Plcd3
Tgfb3
Acta2
Cxcl1#
Ccl8#
Cdkn1a#
Myl9
Ccl21a
Edn1
Flnc
Gabbr1
Traf1
Itpka
Vegfd
Ptpn7
Trbc2
H2-T10
Igf2
Cxcl11#
1 2 3 4
Young control
Doxo control
KSL0608-Se + irradiation

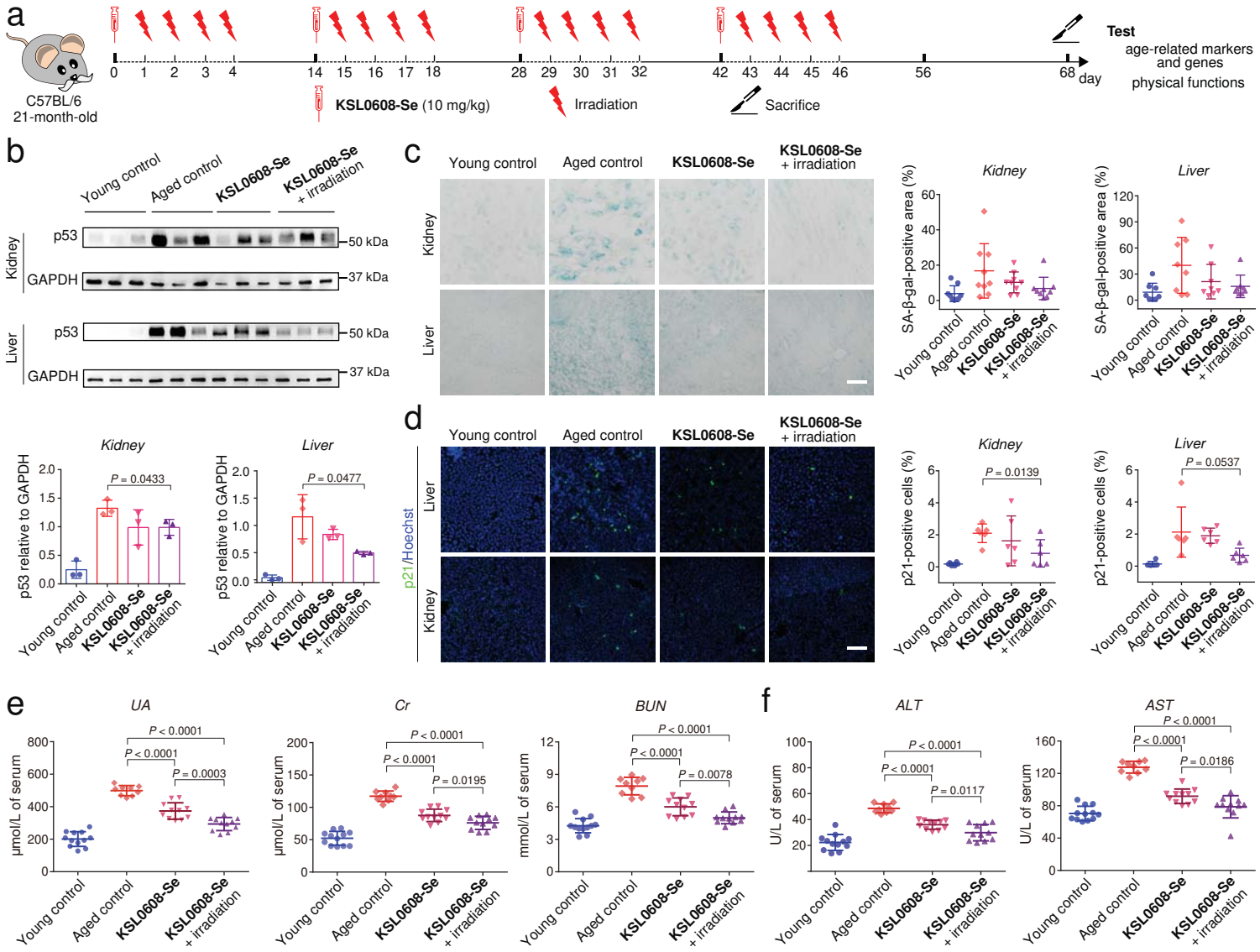
a
C57BL/6
21-month-old
0 1 2 3 4 14 15 16 17 18 28 29 30 31 32 42 43 44 45 46 56 68 day
KSL0608-Se (10 mg/kg)
Irradiation
Sacrifice
Test
age-related markers and genes
physical functions
b
Young control
Aged control
KSL0608-Se
KSL0608-Se + irradiation
Kidney
Liver
p53
GAPDH
50 kDa
37 kDa
p53 relative to GAPDH
P = 0.0433
P = 0.0477
c
SA-β-gal-positive area (%)
d
p21/Hoechst
p21-positive cells (%)
P = 0.0139
P = 0.0537
e
UA
Cr
BUN
μmol/L of serum
mmol/L of serum
P < 0.0001
P = 0.0003
P = 0.0195
P = 0.0078
f
ALT
AST
U/L of serum
P = 0.0117
P = 0.0186

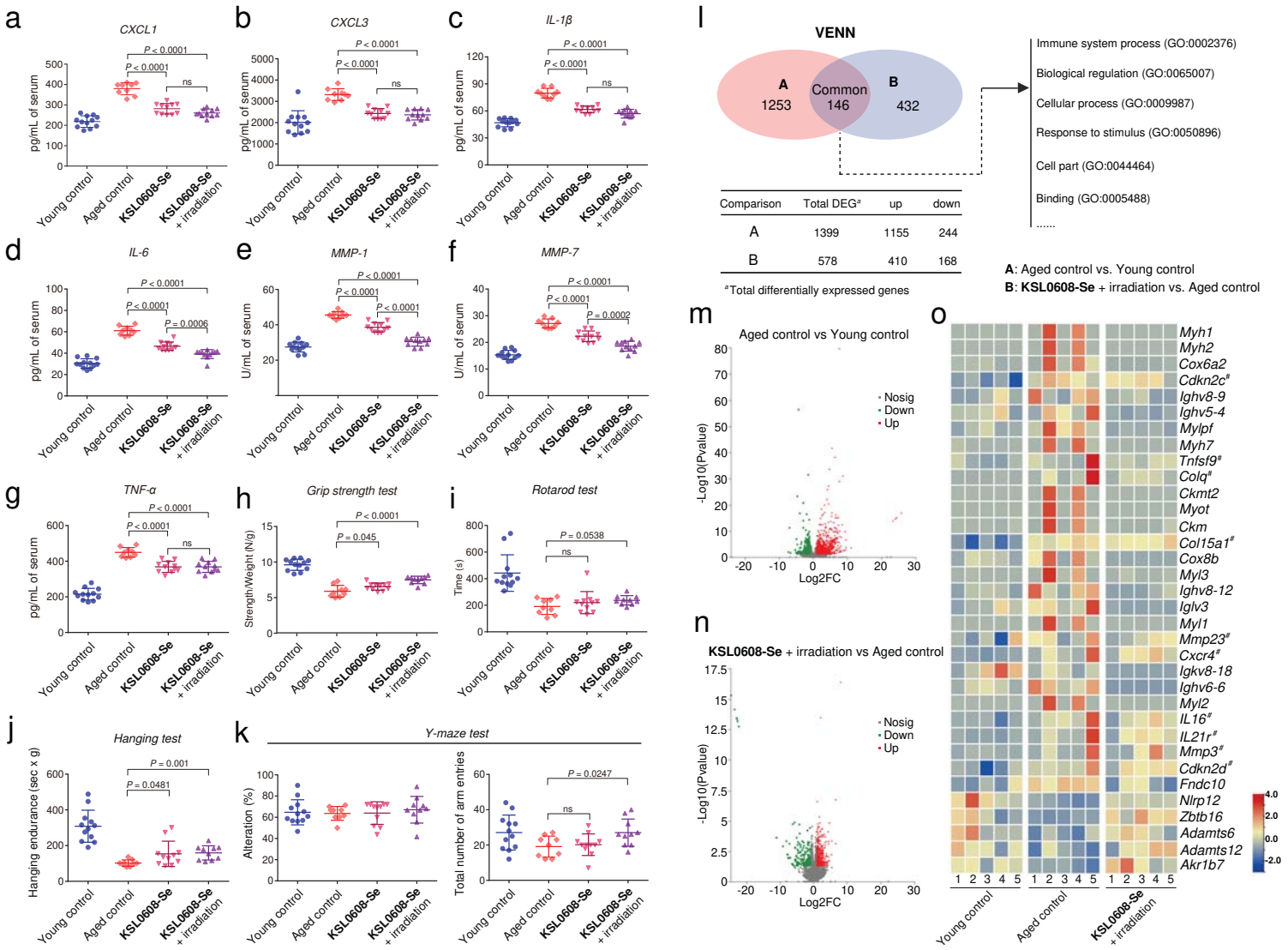
a
CXCL1
b
CXCL3
c
IL-1β
d
IL-6
e
MMP-1
f
MMP-7
g
TNF-α
h
Grip strength test
i
Rotarod test
j
Hanging test
k
Y-maze test
pg/mL of serum
U/mL of serum
Strength/Weight (N/g)
Time (s)
Hanging endurance (sec x g)
Alteration (%)
Total number of arm entries
Young control
Aged control
KSL0608-Se
KSL0608-Se + irradiation
P < 0.0001
P = 0.0006
P = 0.0002
P = 0.045
P = 0.0538
P = 0.001
P = 0.0481
P = 0.0247
ns
l
VENN
A
1253
Common
146
B
432
Immune system process (GO:0002376)
Biological regulation (GO:0065007)
Cellular process (GO:0009987)
Response to stimulus (GO:0050896)
Cell part (GO:0044464)
Binding (GO:0005488)
.....
Comparison
Total DEG#
up
down
A
1399
1155
244
B
578
410
168
#Total differentially expressed genes
A: Aged control vs. Young control
B: KSL0608-Se + irradiation vs. Aged control
m
Aged control vs Young control
n
KSL0608-Se + irradiation vs Aged control
Nosig
Down
Up
-Log10(Pvalue)
Log2FC
o
Myh1
Myh2
Cox6a2
Cdkn2c#
Ighv8-9
Ighv5-4
Mylpf
Myh7
Tnfsf9#
Colq#
Ckmt2
Myot
Ckm
Col15a1#
Cox8b
Myl3
Ighv8-12
Iglv3
Myl1
Mmp23#
Cxcr4#
Igkv8-18
Ighv6-6
Myl2
IL16#
IL21r#
Mmp3#
Cdkn2d#
Fndc10
Nlrp12
Zbtb16
Adamts6
Adamts12
Akr1b7
4.0
2.0
0.0
-2.0
1 2 3 4 5
Young control
Aged control
KSL0608-Se + irradiation

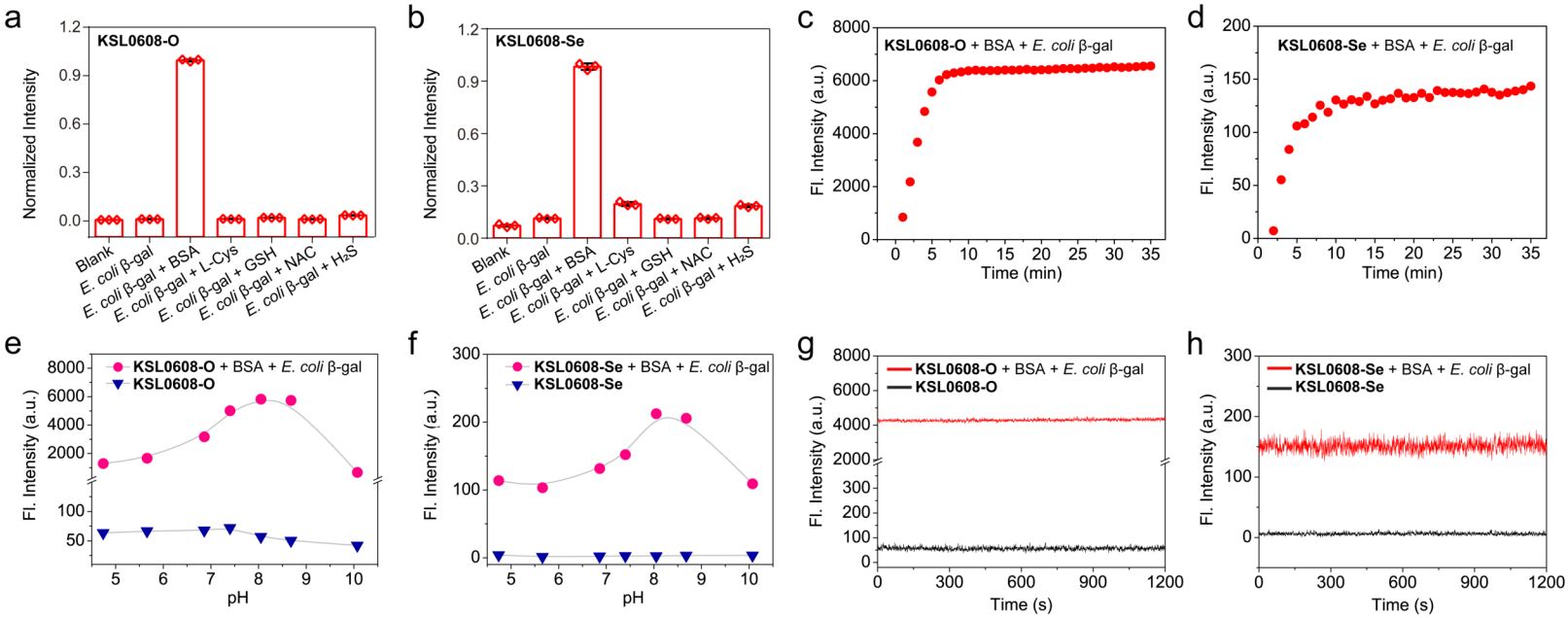
a
KSL0608-O
Normalized Intensity
Blank
E. coli β-gal
E. coli β-gal + BSA
E. coli β-gal + L-Cys
E. coli β-gal + GSH
E. coli β-gal + NAC
E. coli β-gal + H2S
b
KSL0608-Se
c
KSL0608-O + BSA + E. coli β-gal
Fl. Intensity (a.u.)
Time (min)
d
KSL0608-Se + BSA + E. coli β-gal
e
KSL0608-O + BSA + E. coli β-gal
KSL0608-O
pH
f
KSL0608-Se + BSA + E. coli β-gal
KSL0608-Se
g
KSL0608-O + BSA + E. coli β-gal
KSL0608-O
Time (s)
h
KSL0608-Se + BSA + E. coli β-gal
KSL0608-Se

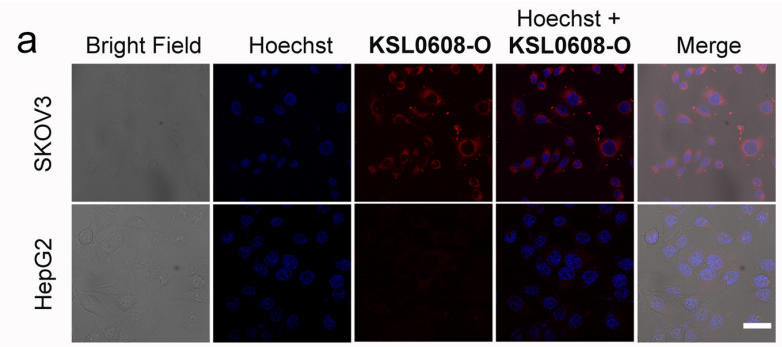
a
Bright Field
Hoechst
KSL0608-O
Hoechst +
KSL0608-O
Merge
SKOV3
HepG2

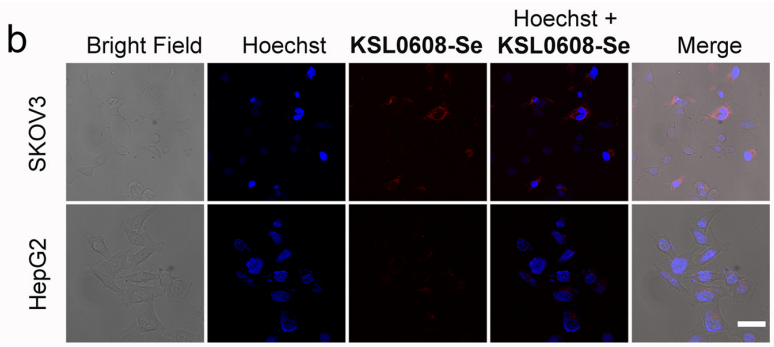
b
Bright Field
Hoechst
KSL0608-Se
Hoechst +
KSL0608-Se
Merge
SKOV3
HepG2

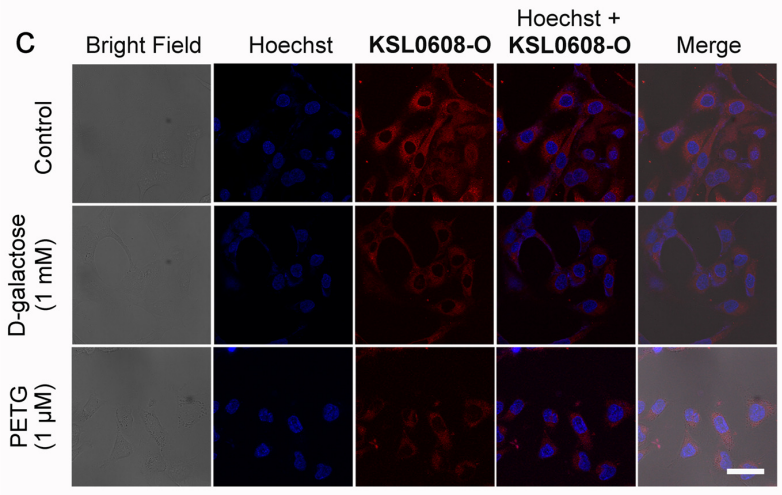
c
Bright Field
Hoechst
KSL0608-O
Hoechst +
KSL0608-O
Merge
Control
D-galactose
(1 mM)
PETG
(1 μM)

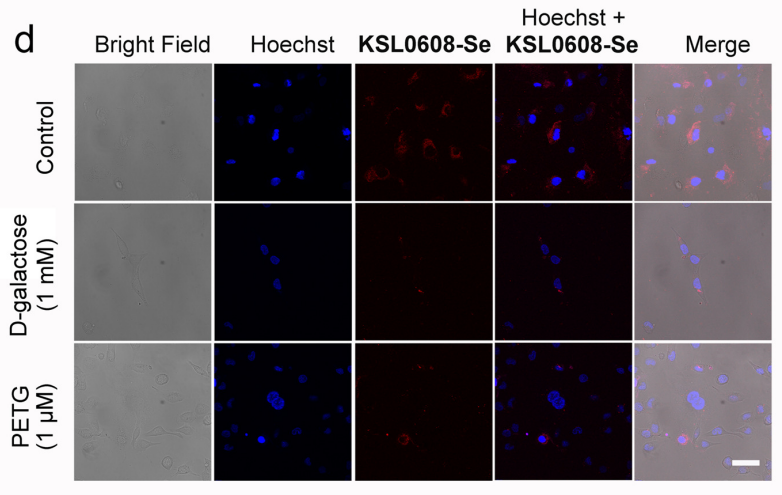
d
Bright Field
Hoechst
KSL0608-Se
Hoechst +
KSL0608-Se
Merge
Control
D-galactose
(1 mM)
PETG
(1 μM)

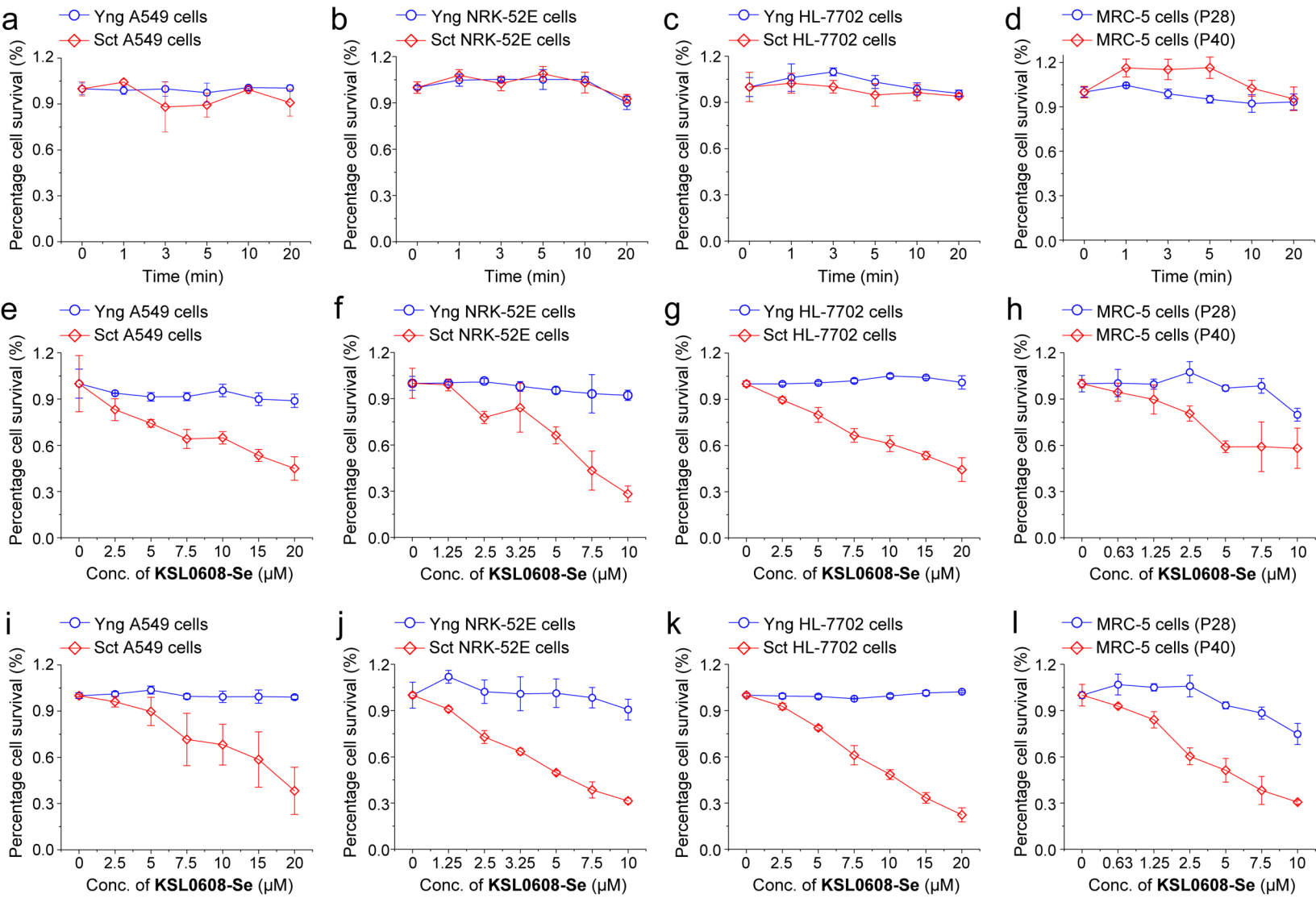
a
Yng A549 cells
Sct A549 cells
Percentage cell survival (%)
Time (min)
b
Yng NRK-52E cells
Sct NRK-52E cells
Percentage cell survival (%)
Time (min)
c
Yng HL-7702 cells
Sct HL-7702 cells
Percentage cell survival (%)
Time (min)
d
MRC-5 cells (P28)
MRC-5 cells (P40)
Percentage cell survival (%)
Time (min)
e
Yng A549 cells
Sct A549 cells
Percentage cell survival (%)
Conc. of KSL0608-Se (μM)
f
Yng NRK-52E cells
Sct NRK-52E cells
Percentage cell survival (%)
Conc. of KSL0608-Se (μM)
g
Yng HL-7702 cells
Sct HL-7702 cells
Percentage cell survival (%)
Conc. of KSL0608-Se (μM)
h
MRC-5 cells (P28)
MRC-5 cells (P40)
Percentage cell survival (%)
Conc. of KSL0608-Se (μM)
i
Yng A549 cells
Sct A549 cells
Percentage cell survival (%)
Conc. of KSL0608-Se (μM)
j
Yng NRK-52E cells
Sct NRK-52E cells
Percentage cell survival (%)
Conc. of KSL0608-Se (μM)
k
Yng HL-7702 cells
Sct HL-7702 cells
Percentage cell survival (%)
Conc. of KSL0608-Se (μM)
l
MRC-5 cells (P28)
MRC-5 cells (P40)
Percentage cell survival (%)
Conc. of KSL0608-Se (μM)

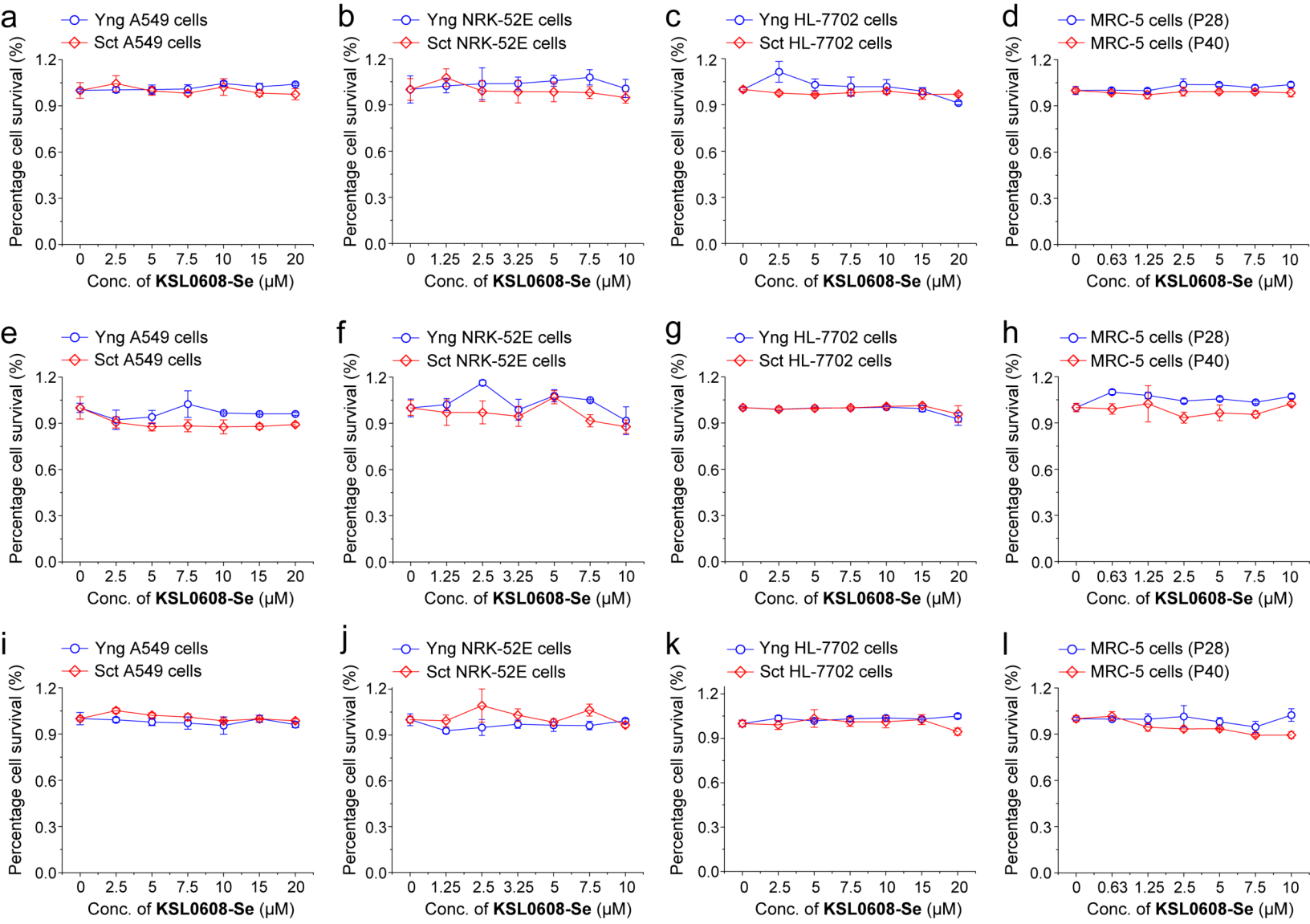
a
Yng A549 cells
Sct A549 cells
Percentage cell survival (%)
Conc. of KSL0608-Se (μM)
b
Yng NRK-52E cells
Sct NRK-52E cells
c
Yng HL-7702 cells
Sct HL-7702 cells
d
MRC-5 cells (P28)
MRC-5 cells (P40)
e
f
g
h
i
j
k
l

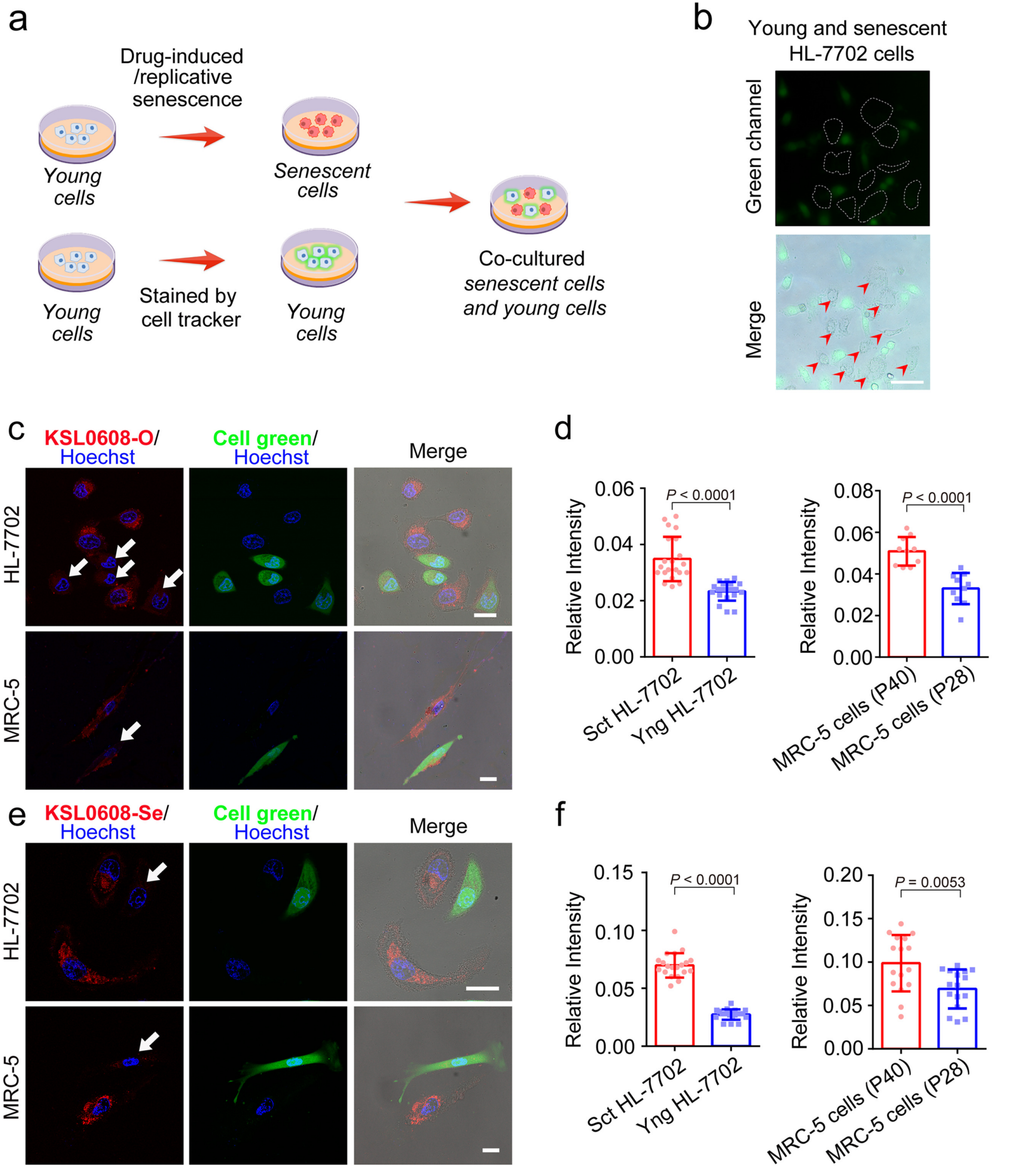
a
Drug-induced
/replicative
senescence
Young
cells
Senescent
cells
Young
cells
Stained by
cell tracker
Young
cells
Co-cultured
senescent cells
and young cells
b
Young and senescent
HL-7702 cells
Green channel
Merge
c
KSL0608-O/
Hoechst
Cell green/
Hoechst
Merge
HL-7702
MRC-5
d
Relative Intensity
0.06
0.04
0.02
0.00
P < 0.0001
Sct HL-7702
Yng HL-7702
0.08
0.06
0.04
0.02
0.00
P < 0.0001
MRC-5 cells (P40)
MRC-5 cells (P28)
e
KSL0608-Se/
Hoechst
Cell green/
Hoechst
Merge
HL-7702
MRC-5
f
Relative Intensity
0.15
0.10
0.05
0.00
P < 0.0001
Sct HL-7702
Yng HL-7702
0.20
0.15
0.10
0.05
0.00
P = 0.0053
MRC-5 cells (P40)
MRC-5 cells (P28)

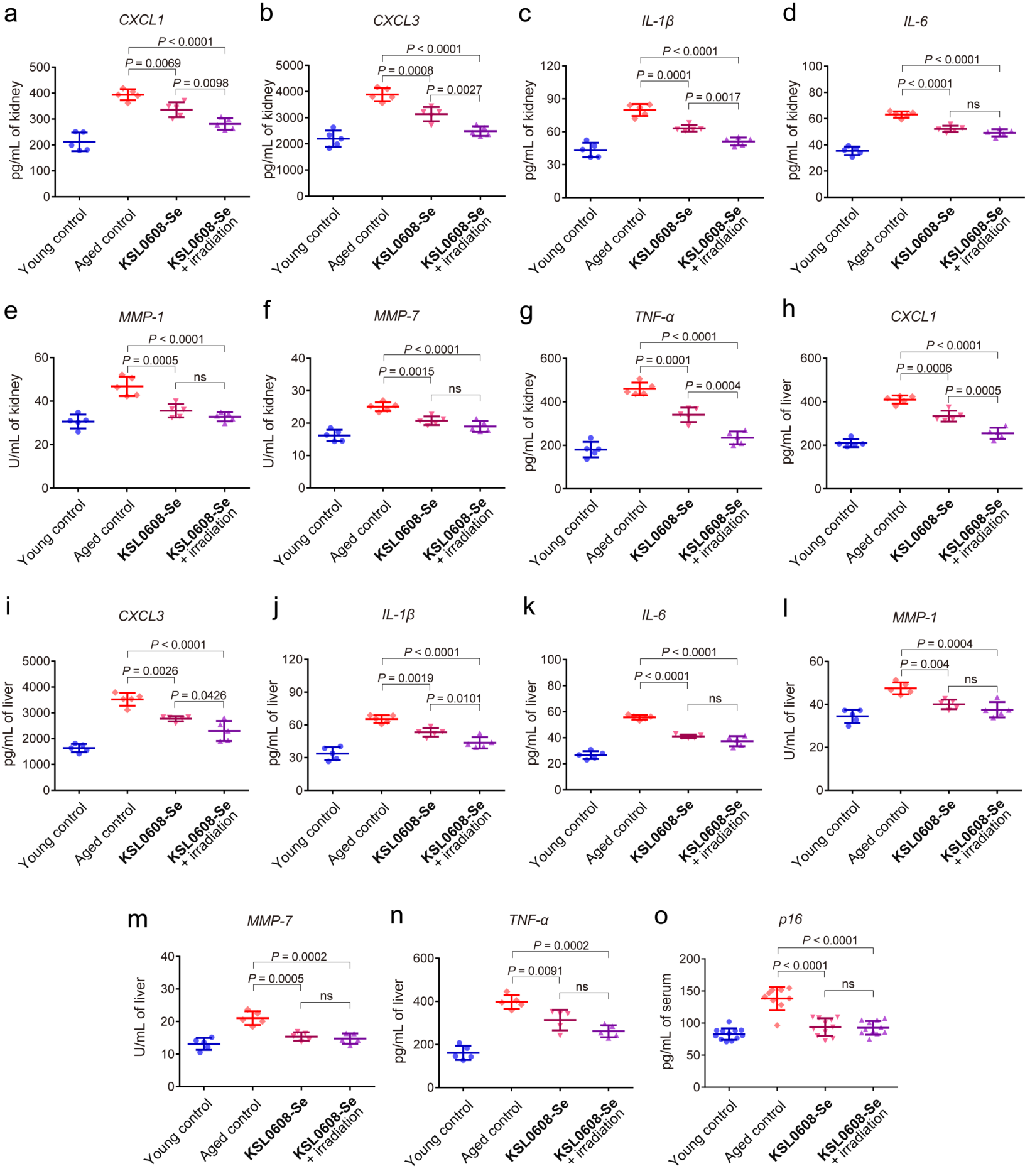
a
CXCL1
pg/mL of kidney
P < 0.0001
P = 0.0069
P = 0.0098
b
CXCL3
pg/mL of kidney
P < 0.0001
P = 0.0008
P = 0.0027
c
IL-1β
pg/mL of kidney
P < 0.0001
P = 0.0001
P = 0.0017
d
IL-6
pg/mL of kidney
P < 0.0001
P < 0.0001
ns
e
MMP-1
U/mL of kidney
P < 0.0001
P = 0.0005
ns
f
MMP-7
U/mL of kidney
P < 0.0001
P = 0.0015
ns
g
TNF-α
pg/mL of kidney
P < 0.0001
P = 0.0001
P = 0.0004
h
CXCL1
pg/mL of liver
P < 0.0001
P = 0.0006
P = 0.0005
i
CXCL3
pg/mL of liver
P < 0.0001
P = 0.0026
P = 0.0426
j
IL-1β
pg/mL of liver
P < 0.0001
P = 0.0019
P = 0.0101
k
IL-6
pg/mL of liver
P < 0.0001
P < 0.0001
ns
l
MMP-1
U/mL of liver
P = 0.0004
P = 0.004
ns
m
MMP-7
U/mL of liver
P = 0.0002
P = 0.0005
ns
n
TNF-α
pg/mL of liver
P = 0.0002
P = 0.0091
ns
o
p16
pg/mL of serum
P < 0.0001
P < 0.0001
ns
Young control
Aged control
KSL0608-Se
KSL0608-Se + irradiation

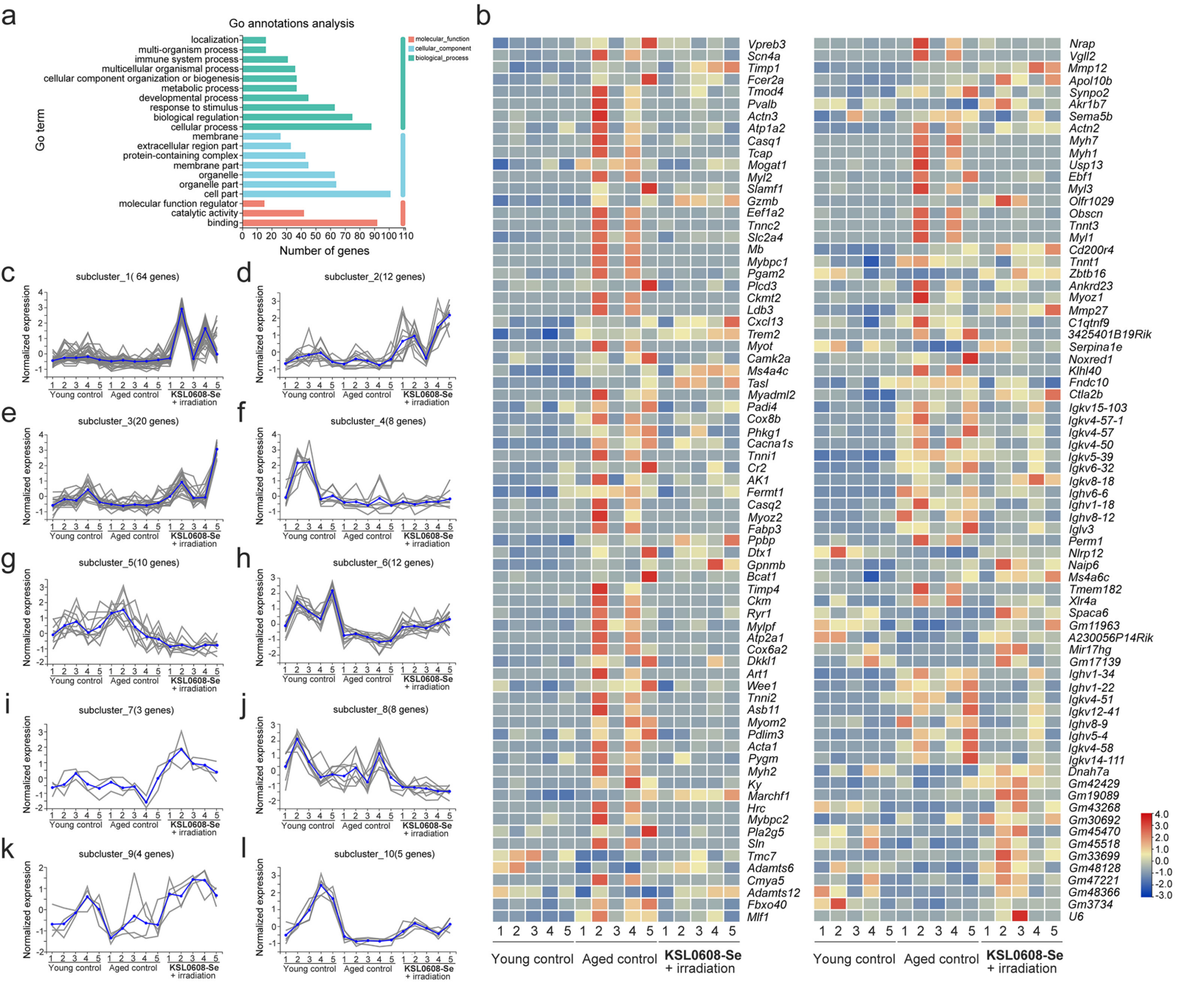
a
Go annotations analysis
Go term
Number of genes
molecular_function
cellular_component
biological_process
localization
multi-organism process
immune system process
multicellular organismal process
cellular component organization or biogenesis
metabolic process
developmental process
response to stimulus
biological regulation
cellular process
membrane
extracellular region part
protein-containing complex
membrane part
organelle
organelle part
cell part
molecular function regulator
catalytic activity
binding
b
c
subcluster_1(64 genes)
d
subcluster_2(12 genes)
e
subcluster_3(20 genes)
f
subcluster_4(8 genes)
g
subcluster_5(10 genes)
h
subcluster_6(12 genes)
i
subcluster_7(3 genes)
j
subcluster_8(8 genes)
k
subcluster_9(4 genes)
l
subcluster_10(5 genes)
Normalized expression
Young control
Aged control
KSL0608-Se
+ irradiation
Vpreb3
Scn4a
Timp1
Fcer2a
Tmod4
Pvalb
Actn3
Atp1a2
Casq1
Tcap
Mogat1
Myl2
Slamf1
Gzmb
Eef1a2
Tnnc2
Slc2a4
Mb
Mybpc1
Pgam2
Plcd3
Ckmt2
Ldb3
Cxcl13
Trem2
Myot
Camk2a
Ms4a4c
Tasl
Myadml2
Padi4
Cox8b
Phkg1
Cacna1s
Tnni1
Cr2
AK1
Fermt1
Casq2
Myoz2
Fabp3
Ppbp
Dtx1
Gpnmb
Bcat1
Timp4
Ckm
Ryr1
Mylpf
Atp2a1
Cox6a2
Dkkl1
Art1
Wee1
Tnni2
Asb11
Myom2
Pdlim3
Acta1
Pygm
Myh2
Ky
Marchf1
Hrc
Mybpc2
Pla2g5
Sln
Tmc7
Adamts6
Cmya5
Adamts12
Fbxo40
Mlf1
Nrap
Vgll2
Mmp12
Apol10b
Synpo2
Akr1b7
Sema5b
Actn2
Myh7
Myh1
Usp13
Ebf1
Myl3
Olfr1029
Obscn
Tnnt3
Myl1
Cd200r4
Tnnt1
Zbtb16
Ankrd23
Myoz1
Mmp27
C1qtnf9
3425401B19Rik
Serpina1e
Noxred1
Klhl40
Fndc10
Ctla2b
Igkv15-103
Igkv4-57-1
Igkv4-57
Igkv4-50
Igkv5-39
Igkv6-32
Igkv8-18
Ighv6-6
Ighv1-18
Ighv8-12
Iglv3
Perm1
Nlrp12
Naip6
Ms4a6c
Tmem182
Xlr4a
Spaca6
Gm11963
A230056P14Rik
Mir17hg
Gm17139
Ighv1-34
Ighv1-22
Igkv4-51
Igkv12-41
Ighv8-9
Ighv5-4
Igkv4-58
Igkv14-111
Dnah7a
Gm42429
Gm19089
Gm43268
Gm30692
Gm45470
Gm45518
Gm33699
Gm48128
Gm47221
Gm48366
Gm3734
U6
4.0
3.0
2.0
1.0
0.0
-1.0
-2.0
-3.0